TU WIEN Informatics

Positioning with 5G reference signals for vehicular applications

DIPLOMARBEIT

zur Erlangung des akademischen Grades

Diplom-Ingenieur

im Rahmen des Studiums

Technische Informatik

eingereicht von

Jan Matthias Nausner, Bsc.

Matrikelnummer 01614835

an der Fakultät für Informatik

der Technischen Universität Wien

Betreuung: Univ.Prof. Ing. Dipl.-Ing. Dr.-Ing. Christoph Mecklenbräuker
Mitwirkung: Univ.Ass. Dipl.-Ing. Mehdi Ashury

Wien, 16. November 2022

_____   _____
Jan Matthias Nausner   Christoph Mecklenbräuker

Technische Universität Wien
A-1040 Wien ▪ Karlsplatz 13 ▪ Tel. +43-1-58801-0 ▪ www.tuwien.at

TU WIEN Informatics

Positioning with 5G reference signals for vehicular applications

DIPLOMA THESIS

submitted in partial fulfillment of the requirements for the degree of

Diplom-Ingenieur

in

Computer Engineering

by

Jan Matthias Nausner, Bsc.
Registration Number 01614835

to the Faculty of Informatics

at the TU Wien

Advisor: Univ.Prof. Ing. Dipl.-Ing. Dr.-Ing. Christoph Mecklenbräuker
Assistance: Univ.Ass. Dipl.-Ing. Mehdi Ashury

Vienna, 16th November, 2022 _____   _____
                                          Jan Matthias Nausner   Christoph Mecklenbräuker

Erklärung zur Verfassung der Arbeit

Jan Matthias Nausner, Bsc.

Hiermit erkläre ich, dass ich diese Arbeit selbständig verfasst habe, dass ich die verwendeten Quellen und Hilfsmittel vollständig angegeben habe und dass ich die Stellen der Arbeit – einschließlich Tabellen, Karten und Abbildungen –, die anderen Werken oder dem Internet im Wortlaut oder dem Sinn nach entnommen sind, auf jeden Fall unter Angabe der Quelle als Entlehnung kenntlich gemacht habe.

Wien, 16. November 2022

_____
Jan Matthias Nausner

v

Danksagung

An erster Stelle möchte ich mich bei meiner Familie und speziell bei meinen Eltern Helena und Günther dafür bedanken, dass sie meine Neugierde und mein technisches Interesse immer gefördert und mir mein Studium an der TU Wien ermöglicht haben. Außerdem möchte ich mich bei meiner Freundin Elena bedanken, die mir in jeder erdenklichen Situation den Rücken stärkt und die mich im Laufe des Verfassens dieser Arbeit stark untersützt hat.

Großer Dank gebührt meinen Studienkollegen Max und Martin, für ihre Freundschaft, für die unzähligen gemeinsamen Lernenstunden und dafür, dass sie das Masterstudium für mich zu einer vegnüglicheren Zeit gemacht haben - speziell während der herausfordernden COVID-19 Pandemie.

Meine tiefe Dankbarkeit gebührt Prof. Mecklenbräuker für das Betreuen meiner Diplomarbeit und für sein wertvolles Feedback. Weiters bin ich sehr dankbar für die unschätzbar wertvolle Unterstützung durch Univ. Ass. Ashury, der meine Forschungstätigkeit im Zuge dieser Arbeit angeleitet und mich immer wieder in die richtige Richtung gedeutet hat. Zum Schluss möchte ich mich bei meinen Kollegen am Institut für Telekommunikation für die vielen spanndenden Diskussionen und für die nette Zeit am Institut bedanken.

Acknowledgements

First and foremost, I want to thank my family, especially my parents Helena and Günther, for always supporting my curiosity and technical interests and for enabling my academic studies at TU Vienna. Furthermore, I want to thank my girlfriend Elena for having my back in every thinkable situation and for strongly supporting me throughout my work on this thesis.

Big thanks to my fellow students Max and Martin for their friendship, for the countless hours of joint studying and for making the master studies a more pleasurable experience - especially during the challenging COVID-19 pandemic.

My sincere gratitude goes to Prof. Mecklenbräuker for supervising my thesis and providing me with valuable feedback. I am also very grateful for the invaluable support by Univ. Ass. Ashury, who guided my research for this thesis in countless meetings and helped to point me in the right directions. Finally, I also want to thank my colleagues at the Insitute of Telecommunications for many interesting discussions and for making the time at the institute enjoyable.

Kurzfassung

Moderne sicherheitskritische Fahrzeuganwendungen wie autonomes Fahren oder Advanced Driver Assistance Systems (ADAS) benötigen genaue Information über die Position des Fahrzeuges. Sensorbasierte Positionierungsmethoden wie Global Satellite Navigation Systems (GNSS), Radio/Light Detection and Ranging (RADAR/LiDAR) oder Kamerasysteme sind gut erforscht und können eine hohe Positionsgenauigkeit erreichen, haben aber ihre spezifische Schwächen. Die Positionsgenauigkeit von GNSS verringert sich stark in urbanen Gegenden und RADAR/LiDAR bzw. Kamerasysteme benötigen zur globalen Positionierung dreidimensionale Karten der Umgebung auf Basis von Punktwolken und rechenintensive Algorithmen, nur um einige Nachteile zu nennen. Kooperative, Vehicle-to-Infrastructure (V2I) Positionierung im gerade aufkommenden Mobilfunknetz der 5. Generation (5G-NR) ist ein Technologiekandidat für genaue und verlässliche Fahrzeugpositionierung aufgrund von erhöhter Bandbreite, der Unterstützung des Millimeterwellenbandes (mmWave) und der Verdichtung des Mobilfunknetzes, hat aber bisher nur moderate Aufmerksamkeit der Forschungsgemeinschaft für diese konkrete Anwendung bekommen. In dieser Arbeit untersuchen wir die Positionierung mittels Time Difference of Arrival (TDOA) mit 5G-NR standardkonformen Referenzsignalen. Ein besonderer Fokus liegt hier auf Situationen ohne Sichtverbindung und mit Mehrwegeausbreitung, da diese in (sub-)urbanen Fahrzeugszenarien vorherrschend sind. Zu diesem Zweck präsentieren wir verschiedenen Techniken zur Schätzung von Verzögerungsprofilen und Methoden zur Detektion der Verzögerung des direkten Pfades um eine genaue Schätzung der Signalverzögerung und somit der Entfernung zur ermöglichen. Weiters vergleichen wir die Genauigkeit der Techniken mittels MATLAB-Simulationen. Darauf aufbauend zeigen wir Methoden zur Lösungsapproximation des hyperbolischen Positionierungsproblems, welches als Resultat der TDOA-Messung entsteht. Die Genauigkeit der Methoden wird in Situationen ohne Sichtverbindung und mit Mehrwegeausbreitung mittels Simulationen verglichen. Zum Abschluss fügen wir ein Ende-zu-Ende Positionierungssystem auf Basis der bestgeeigneten Methoden zusammen. Um das System zu evaluieren, konstruieren wir ein Fahrzeugszenario basierend auf der Geometrie in der realen Welt und simulieren die Positionierungsgenauigkeit entlang einer Fahrzeugtrajektorie. Die Resultate bestätigen, dass unser vorgeschlagenes System in der herausfordernden Umgebung des Szenarios genaue Positionsinformation bereitstellen kann.

Abstract

State-of-the-art safety-critical vehicular applications like autonomous driving or advanced driver assistance systems (ADAS) require accurate knowledge of the vehicle position. Sensor-based positioning methods such as global satellite navigation systems (GNSS), radio/light detection and ranging (RADAR/LiDAR) or camera systems are well-studied and can provide high positioning accuracy, but have their specific weaknesses. The performance of GNSS positioning severely degrades in urban environments, while RADAR/LiDAR or camera systems require three-dimensional point cloud maps and computationally expensive algorithms in order to perform global positioning, only to name a few drawbacks. Cooperative, vehicle-to-infrastructure (V2I) positioning in the upcoming 5th generation cellular network (5G-NR) is a candidate technology for accurate and reliable vehicular positioning due to increased bandwidth, support for the millimeter wave band (mmWave) and network densification, but has up until now received less attention from the research community for this particular application. In this work, we investigate time difference of arrival (TDOA) positioning with 5G-NR standard-compliant reference signals, with a strong focus on non line of sight (NLOS) and multipath propagation prevalent in (sub-)urban vehicular scenarios. For this purpose, we introduce various delay profile estimation techniques and direct path delay peak detection methods in order to perform accurate time delay and range estimation and compare their performance with MATLAB simulations. Based on that, we show methods for approximately solving the hyperbolic positioning problem arising from the TDOA measurements and compare their performance based on simulations in NLOS and multipath-heavy situations. Finally, we construct an end-to-end positioning framework comprised of the best-suited methods. In order to evaluate this framework, we build an urban vehicular scenario based on real-world geometry data and simulate the positioning accuracy along a vehicular trajectory. The results confirm that our proposed positioning framework is capable of providing accurate position information in the harsh propagation environment encountered in the simulation scenario.

Contents

CHAPTER 1

Introduction

The ever increasing demand for personal mobility and transportation in the current and previous century lead to a steadily increasing road traffic volume in Austria - in part due to the still growing individual traffic sector [AST]. This gives rise to many challenges such as increased pollution, road congestion and traffic accidents. Altough the numbers have been decreasing in the past, in 2021 alone 359 people died in Austria due to road traffic accidents [STV] and many more have been injured. Current research and development focuses on trying to tackle many of the problems associated with individual road traffic with emerging, safety-critical vehicular applications like autonomous driving and advanced driver assistance systems (ADAS). One thing that systems such as navigation, automatic lane changing and keeping, collision avoidance and automated parking have in common is that they require accurate knowledge of the vehicle position. State-of-the-art vehicular positioning techniques can be broadly classified into the following categories [KFK$^+$18]:

- *Sensor-based positioning methods.* A sensor (or a combination of multiple sensors) mounted on the vehicle perceives its environment and based on the recorded data the global position of the vehicle can be computed.

- *Cooperative positioning methods.* The vehicle communicates with its environment and exchanges positioning-related data with other adjacent road users or with infrastructure at fixed positions in order to determine its global position.

Sensor-based positioning methods include various global navigation satellite system (GNSS), which have enabled vehicular positioning in the last decades, but suffer from reliability issues and lowered accuracy especially in urban environments. Other sensor systems such as radio detection and ranging (RADAR), light detection and ranging (LiDAR) or cameras can perform measurements of obstacle ranges and are able to achieve very high vehicular positioning accuracy. However, the major challenge arising with such

systems is that they require a three-dimensional point cloud map of the environment in order to perfom global positioning by correlating the sensor data with a map. Generating such maps involves resource intensive tasks like data collection, analysis and maintenance and the associated simultaneous localization and mapping (SLAM) and map-matching algorithms are computationally expensive. Futhermore, positioning accuracy might be diminished by environment variations not refelcted by the map, obstructions, interference or bad weather conditions.

One type of cooperative technique is referred to as vehicle-to-vehicle (V2V) positioning, where adjacent vehicles transmit and receive wireless signals from each other. Based on parameters like signal propagation time or angular measurements, the ranges between the vehicles or, if multiple signals are available, the relative positions can be computed. Furthermore, vehicles might exchange position information via ad-hoc wireless connections in order to perform cooperative mapping. These methods however require an additional system that provides self-localization, such that the relative positions can be put into the context of a global coordinate system. The positioning accuracy strongly depends on factors such as communication latency and faults, vehicle movement and line of sight (LOS) availability. Another cooperative method is known as vehicle-to-infrastructure (V2I) positioning. Here the vehicle communicates with wireless network infrastructure such as road side units (RSUs) or cellular network base stations (BSs). Again, based on signal propagation time, angular measurements or other parameters, the global position of the vehicle in the network can be determined. As in V2V systems, positioning related data can be shared with other road users over the network infrastructure. V2I positioning has a potential for high accuracy and reliability, however complex and expensive network infrastructure is required and accuracy might severly degrade if effects of non line of sight (NLOS) propagation cannot be mitigated or used favorably by the positioning algorithm.

In this thesis, we investigate cooperative positioning techniques based on the upcoming 5th generation cellular network - new radio (5G-NR) technology. Several key properties make 5G-NR-based positioning a promising candidate for high-accuracy positioning [ZLWW17]:

- Large bandwidths in the order of hundreds of MHz, reducing latency and increasing time measurement accuracy with improved ranging quality as a consequence.

- High carrier frequencies in the millimeter wave band (mmWave) around 30 GHz, allowing for large antenna arrays with strong beamforming and signal estimation capabilities and a sparse channel with regard to multipath components.

- High-speed, low-latency data exchange not only between mobile users and the cellular base stations, but also directly between mobile devices, known as device-to-device (D2D) communication.

Furthermore, it is expected that the roll-out of 5G-NR comes with a densification of the cellular network, leading to an increased number of available reference points and a higher

probability for line of sight (LOS) connections [ZLWW17]. This would be beneficial for positioning especially in urban areas, where conventional GNSS tends to struggle the most. Since 5G-NR network infrastructure is currently being implemented around the world for communication purposes, a potential reduction of the high initial cost of V2I positioning is expected if existing infrastructure can be used. Additionally, we highlight that several different positioning methods have already been specified in the 3rd generation partnership project (3GPP) standard for 5G-NR [rGPPG22]. Compared to other positioning techniques listed above, up until now vehicular positioning in 5G-NR network has received less attention from the research community. In the course of this thesis, we investigate and benchmark different methods for positioning in 5G-NR networks. Based on our findings we propose a positioning method relying on propagation time parameters and show its applicability to vehicular scenarios, especially focusing on situations with a high probability for NLOS links. In order to evaluate the proposed algorithms we develop a suitable MATLAB simulation framework incorporating the various required system models.

In general it should be stated that a highly accurate and reliable vehicular positioning framework of the future will likely not comprise of only a single method, but rather combine multiple of the techniques and approaches introduced above in order to make up for the different weaknesses and to benefit from all the strengths specific to the individual methods.

1.1   Thesis structure

This thesis is organized as follows: Chapter 2 gives the reader an overiew over the positioning problem in cellular networks. The potentially available positioning parameters are listed and positioning approaches making use of these parameters are presented. In chapter 3, a transmission system model for the 5G-NR physical layer is introduced, where special attention is paid to modelling NLOS propagation channels. Furthermore, the specification and behavior of a 3GPP standard-compliant reference signal for positioning is outlined. Building on top of this system model, several methods for delay profile estimation and delay peak detection are introduced and applied to the problem at hand - for the purpose of estimating propagation time delay. The different methods are evaluated in a simulation framework and their performance is compared based on the simulation results. Chapter 4 introduces the problem of position estimation based on time difference of arrival (TDOA) measurements. Methods for solving this problem are presented and their performance is compared based on simulations. In chapter 5, the complete 5G-NR vehicular positioning framework constructed by the previous chapters is applied to a simulation scenario based on real-world geometry and the resulting positioning performance is evaluated. Finally, in chapter 6 the findings obtained in the course of this thesis are summarized and hints for possible future work are given.

1.2   Notation

In this thesis, column vectors are denoted by bold lowercase letters and matrices are denoted by bold uppercase letters. The following notations are used for matrices with special structure: $\boldsymbol{I}_{n \times m}$ denotes the $n \times m$ identity matrix, $\boldsymbol{0}_{n \times m}$ denotes an $n \times m$ matrix filled with zeros, $\boldsymbol{1}_{n \times m}$ denotes an $n \times m$ matrix filled with ones and $\text{diag}\{\cdot\}$ defines a matrix where the main diagonal is filled with the argument vector elements and the elements outside the main diagonal being set to zero. Futhermore, various matrix operations are used: $(\cdot)^T$ for matrix transpose, $(\cdot)^H$ for matrix Hermitian, $||\cdot||_2$ for the Euclidean or l^2 vectornorm. The operator $*$ refers to the linear convolution, $\circledast$ to the circular convolution, $\circ$ signifies the Schur product and $\mathcal{E}\{\cdot\}$ denotes the linear expectation operation. The conjugate of a complex number is expressed by the notation $(\cdot)^*$, the floor operation $\lfloor \cdot \rfloor$ rounds towards minus infinity and $a \bmod b$ denotes the integer operation a modulo b.

<div style="text-align:right">CHAPTER 2</div>

Donwlink positioning methods for cellular networks

The following chapter introduces the positioning problem underlying this whole thesis. The focus is on positioning methods for cellular networks, where the BSs transmit reference radio signals and the receiving user equipment (UE) computes its own position based on the received signals - hence we focus on downlink positioning only. Note however, since 5G-NR allows for bidirectional communication, there also exist methods for uplink, or network-based positioning as well as combined downlink and uplink positioning, which are not subject of this thesis. In this chapter, we outline the state of the art and show which different positioning parameters can be estimated in a cellular network and how these parameters are used to estimate the UE position.

The chapter is structured as follows: Section 2.1 introduces the downlink positioning problem in cellular networks. In section 2.2, it is explained how the propagation time of the emitted radio signal can be used to derive range information in order to estimate the position of the UE, while the methods in section 2.3 rely on angular measurements to solve the positioning problem. Section 2.4 introduces positioning methods based on measurement of received signal strenght. In section 2.5 we present modern, emerging ideas for positioning in cellular networks, which are still in early development but appear to be promising approaches. Finally, section 2.6 introduces the ideas of filtering and sensors fusion to provide options for increasing the accuracy of positioning systems.
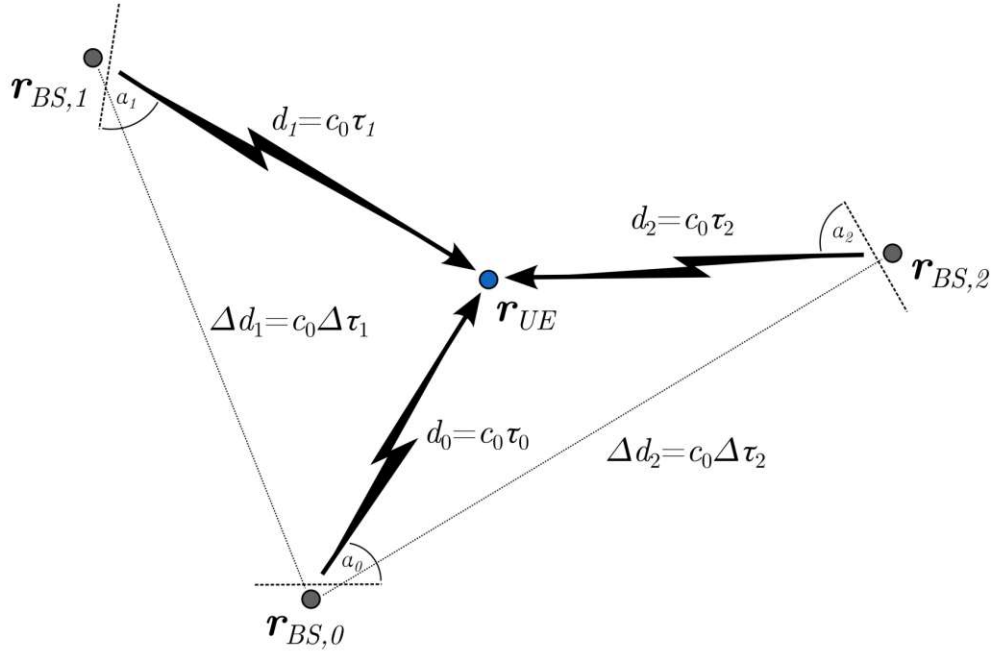
5

Figure 2.1: Parameters for downlink positioning in cellular networks supported by the 3GPP standard, $N_{BS} = 3$

2.1 Problem statement

Consider a cellular network with N_{BS} BSs at arbitrary but known positions $\boldsymbol{r}_{BS,i} \in \mathbb{R}^{dim \times 1}$, $i = 0 \ldots N_{BS} - 1$, where each is transmitting reference radio signals on downlink, which are also known. The parameter $dim \in \{2, 3\}$ denotes the dimensionality of the coordinate system. Furthermore, there is a receiving UE located at the unknown position $\boldsymbol{r}_{UE} \in \mathbb{R}^{dim \times 1}$. The task is now to estimate the position $\boldsymbol{r}_{UE}$, which is carried out in a two-step process. First, one or multiple sets of parameters available in this constellation are estimated. In a second step, the UE position is estimated by employing an appropriate positioning method. The following positioning parameters can be measured in this setup [PAK+05, ZB11]:

- The time delays due to the radio signal propagation $\tau_0, \ldots, \tau_{N_{BS}-1}$, which yield the transmitter-recveiver ranges $d_0, \ldots, d_{N_{BS}-1}$ via the propagation speed c_0[1], as in $d_i = ||\boldsymbol{r}_{BS,i} - \boldsymbol{r}_{UE}||_2 = c_0 \tau_i$.

- The time delay differences $\Delta \tau_0 = \tau_0 - \tau_j, \ldots, \Delta \tau_{j-1} = \tau_{j-1} - \tau_j, \Delta \tau_{j+1} = \tau_{j+1} - \tau_j, \ldots, \Delta \tau_{N_{BS}-1} = \tau_{N_{BS}-1} - \tau_0$ for the reference transmitter at $\boldsymbol{r}_{BS,j}$ yield the

---

[1]speed of light, $c_0 = 299792458 \ \frac{m}{s}$

range differences $\Delta d_1, \ldots, \Delta d_{j-1}, \Delta d_{j+1}, \ldots, \Delta d_{N_{BS}-1}$ of those transmitters, via the above relationship.

- The angles of departure $\alpha_0, \ldots, \alpha_{N_{BS}-1}$ at the transmitters.

- The signal strengths at the receiver, which again yield the transmitter-recveiver ranges $d_0, \ldots, d_{N_{BS}-1}$.

The positioning problem and the parameters listed above are visualized in figure 2.1 for a setup with $N_{BS} = 3$ transmitting BSs. Note that the short dashed lines represent arbitrary planes serving as a reference for measuring the angles - they could be the antenna baseplanes in practice, for example. Furthermore, the dotted lines represent range differences, while the arrows symbolize the downlink signals which propagate over the respective transmitter-recveiver distances.

The following sections 2.2, 2.3 and 2.4 are based on [PAK$^+$05, ZB11].

2.2 Propagation time based methods

2.2.1 Time of arrival measurements

The time of arrival (TOA) of a signal is the transmission time of the signal plus the propagation time due to the distance d between transmitter and receiver. Hence in order to extract the time delay τ which is required to compute the distance $d = c_0\tau$, the receiver must know the exact transmission time of the signal, or, in other words, receiver and transmitter must be perfectly synchronized. Disturbances of the time delay estimates occur due to additive noise during the transmission. Another major source of error is multipath propagation, i.e. the attenuation and reflection of the transmit signal due to blocking objects. The direct signal component might be severly attenuated and thus lost in noise. This could lead to a reflected signal being picked up at the receiver instead of the direct signal, which would yield a biased range estimate. Chapter 3 includes a more in-depth explanation of the time delay estimation problem with a focus on multipath-heavy environments and presents several methods that are able to measure time delay.

2.2.2 Time difference of arrival measurements

In order to circumvent the strong assumption about perfect receiver-transmitter synchronization imposed by the TOA method, a common approach is to instead measure the TDOA for multiple different transmitters. Hence for a network with N_{BS} transmitters, an arbitrary BS j, with $0 \le j < N_{BS}$, is selected as a time reference to compute the TDOAs $\Delta\tau_i = \tau_i - \tau_j$, with $0 \le i < N_{BS}$, $i \ne j$. This idea drops the receiver-transmitter synchronization assumption and only requires time synchronization between transmitters, however at the cost of sacrificing one transmitting station as a time reference. The TDOA values yield the range differences $\Delta d_i = c_0\Delta\tau_i - \tau_j$, with $0 \le i < N_{BS}, i \ne j$. Of course

this method is, much like the TOA method, also negatively affected by additive noise and multipath propagation.

2.2.3 Lateration

Assuming that N_{BS} range measurements d_i, $0 \leq i < N_{BS}$ are available at the receiving UE as a result of the TOA method, the ranges can be used to define circles, with the respective centers being at the BS positions $\boldsymbol{r}_{BS,i}$ and with each corresponding circle having radius d_i. If $N_{BS} = 1$, there are infinite possibilites for the UE position $\boldsymbol{r}_{UE}$, however they are restricted to lie on the circle around the BS. In the case of $N_{BS} = 2$ (*bilateration*), there are two circles available, which might intersect in one or two points, hence adding a second BS already drastically reduces the number of possible UE positions. If the number of transmitters is increased to $N_{BS} = 3$ (*trilateration*), or even further to $N_{BS} > 3$ (*multilateration*), the circles all intersect at a single point, instantly leading to a unique UE position. In case the transmitted signals are corrupted by additive noise or multipath propagation, the circles might not overlap in a single point or even not at all, giving rise to the need for approximate method to solve the set of circular equations. Note that these explanations assume the two-dimensional positioning case with $dim = 2$. For $dim = 3$, the circles become spheres and $N_{BS} \geq 4$ is required to obtain a unique solution for the UE position. Note that this method is not supported by the 5G-NR standard [rGPPG22], hence it will not be considered further in this thesis.

In case the TDOA method is employed and N_{BS} range difference values Δd_i, $0 \leq i < N_{BS}$, $i \neq j$ with respect to the reference BS $\boldsymbol{r}_{BS,j}$ are measured at the receiving UE, the range differences now define define hyperbolas on which the UE position $\boldsymbol{r}_{UE}$ must lie. As stated before, lateration with TDOA values requires one additional BS as compared to lateration with TOA values. Therefore, at least $N_{BS} = 4$ transmitters are required to obtain a unique solution for the UE position $\boldsymbol{r}_{UE}$ in the two-dimensional case with $dim = 2$. Hence when TDOA measurements are used, usuall only the term *multilateration* is used to describe the positioning process. In the three-dimensional case with $dim = 3$, the hyperbolas becom hyperboloids and $N_{BS} = 5$ BSs are required in order to obtain a unique solution. Of course it is possible to use even more measurements, which is especially desirable in situations with additive noise or multipath propagation, where approximate solutions to the hyperbolic set of equations must be found. The TDOA approach is supported by the 5G-NR standard [rGPPG22] and a more elaborate discussion of hyperbolic positioning can be found in chapter 4.

2.3 Angle based methods

2.3.1 Angle of departure measurements

The angle of departure (AOD) α of a reference signal at the transmitter can be estimated using smart antennas and reference signal received power (RSRP) reports with fingerprinting [KSHK19]. The term *smart antenna* refers to the pairing of antenna arrays

with signal processing algorithms such as beamforming. The measured AOD value is then transmitted to the UE in order to be made available to the subsequent positioning algorithm. AOD information is complementary to TOA or TDOA information as it provides hints about the direction of the UE relative to the BS, rather than the range or range differences. The downlink AOD approach is supported by the 5G-NR standard [rGPPG22]. Note that it is also feasible to measure the angle of arrival (AOA) of a reference signal at the receiver, using antenna arrays combined with algorithms that estimate the incident angle, for example based on the phase delay. The challenge in this setting is that without further sensors such as e.g. a compass, neither position nor orientation of the receiver are known. Furthermore, the downlink AOA approach is not supported by the standard [rGPPG22]. As with methods based on propagation time, major disturbances of angular measurements occur due to additive noise and multipath propagation.

2.3.2 Angulation

Given N_{BS} AOD measurements α_i, $0 \leq i < N_{BS}$ at the UE, the UE position can be computed by defining lines of bearing based on the respective BS positions $\boldsymbol{r}_{BS,i}$ and the measured AODs. The UE position $\boldsymbol{r}_{UE}$ is situated at the intersection of the bearing lines. $N_{BS} = 2$ transmitters are sufficient to obtain a unique solution (*biangulation*). $N_{BS} = 3$ (*triangulation*) or $N_{BS} \geq 3$ (*multiangulation*) transmitters are favorable in situations where the AOD measurements are disturbed by additive noise or multipath propagation, because bearing lines might not intersect in a single point, hence giving rise to the need for approximate solution methods. In case the three-dimensional positioning problem shall be solved, it is required that in addition to the AODs the respective elevation angles are estimated, however two transmitters are still sufficient to obtain a unique solution in the noise and distortion free scenario. Since in this thesis we do not employ antenna arrays and focus on propagation time based positioning in the single input single output (SISO) case, the angular approach will not be considered further.

2.4 Received signal strength based methods

Another approach is to measure the received signal strength (RSS) at the receiver. Based on the known transmit power, the measured RSS and an appropriate path loss model describing how the reference signal power decreases with the square of the distance and due to the propagation environment, the range between transmitter and receiver can be estimated. In a second step, the position of the UE can be computed by lateration, much like with TOA measurements. An advantage of this method is that in principle it does not require any time synchronization between network elements. Major sources of error for this method are multipath propagation, where multiple received signal reflections interfere with each other, as well as signal attenuation due to blocking objects. Therefore, the accuracy of RSS based positioning highly depends on the accuracy and applicability

of the employed path loss model. Note that this method is not supported by the 5G-NR standard [rGPPG22], hence it is not considered further in this thesis.

2.5   Emerging methods

Since 5G-NR is expected to support technologies such as millimeter wave (mmWave) or massive multiple input multiple output (MIMO) [BHL$^+$14], it provides the opportunity for the development and potential deployment of novel positioning methods making use of the newly introduced network features. The main idea is that technologies like mmWave or massive MIMO allow multipath propagation to be viewed as a valuable source of information for the positioning process rather than an undesirable disturbance [WML$^+$16]. The work in [WKWW20] proposes a tensor-based channel estimation algorithm that is able to determine delays and angles of all individual components in a multipath propagation environment. Building on this method, [GWK$^+$20] presents an end-to-end positioning framework that employs a SLAM algorithm to construct an environment map of signal reflection and scattering points, referred to as virtual anchors. These virtual anchors are used as reference points to achieve sub-meter positioning accuracy using only a single transmitting BS at the cost of high computational complexity. In [KWG$^+$18, KGG$^+$20], these ideas are applied to vehicular scenarios, demonstrating the feasibility of high accuracy vehicular positioning and tracking in multipath environments with reference signals from only a single BS. These emerging methods are listed for completeness and their futher investigation is not a subject of this thesis.

2.6   Filtering and sensor fusion

In order to achieve an accurate and reliable positioning system, especially in dynamic situations such as positioning of a moving vehicle, it is desirable to apply filtering methods and to perform sensor fusion [Mit12]. Filtering in this sense refers to a state estimation process where the next system state is predicted according to a state transition model and then updated and corrected based on sensor readings giving indication of the actual current system state. In case of vehicular positioning, the system state comprises of the current position and speed, while the state transition model would be a kinematic model of the vehicle. The advantage brought by filtering is that it can provide relatively accurate system state estimation even in situations where the sensor readings are not realiable, such as in case of bad signal reception in tunnels or cluttered environments. Common filtering methods include the well-known Kalman filter or the particle filter. Sensor fusion refers to an approach where readings from different sensors are combined to achieve increased state estimation performance. An example applicable to cellular networks would be to perform joint positioning based on TDOA as well as AOD measurements. Note that any types of appropriate sensors can be fused. For the application of vehicular positioning, this might include systems such as RADAR [AEBM20], GNSS [MSD10, MGA$^+$20] or other state-of-the-art sensor suites [KFK$^+$18]. Due to the diversity, sensor fusion allows to compensate for weaknesses of individual sensor systems and hence is able to increase

accuracy and reliability of the positioning system. Filtering and sensor fusion are however not in the scope of this thesis.

CHAPTER 3

Time delay measurement with 5G reference signals

Since the focus of this thesis is on positioning methods using timing information, methods for measuring propagation time, or equivalently the range, between BS and UE are required. The following chapter investigates how such measurements can be conducted in 5G-NR cellular networks by employing standard compliant reference signals. Special attention is paid to environments with difficult propagation conditions that can be found in urban regions for example, which are a common field for vehicular applications. Time delay estimation with sufficient accuracy is particularly challenging in environments like that.

This chapter is structured as follows: Section 3.1 introduces the system model for transmitting and receiving standard-compliant 5G-NR reference signals suitable for positioning applications. An emphasis is put on modelling propagation channels and propagation delay. Section 3.2 presents the challenges of delay estimation in urban environments and introduces the components of a suitable delay estimation procedure. Section 3.3 introduces various methods for estimating delay profiles of a multipath channel, while section 3.4 shows methods for detecting delay peaks from such delay profiles. Finally, section 3.5 introduces the simulation setup and standard-compliant channel models. Furthermore, it summarizes the simulation results and their interpretation.
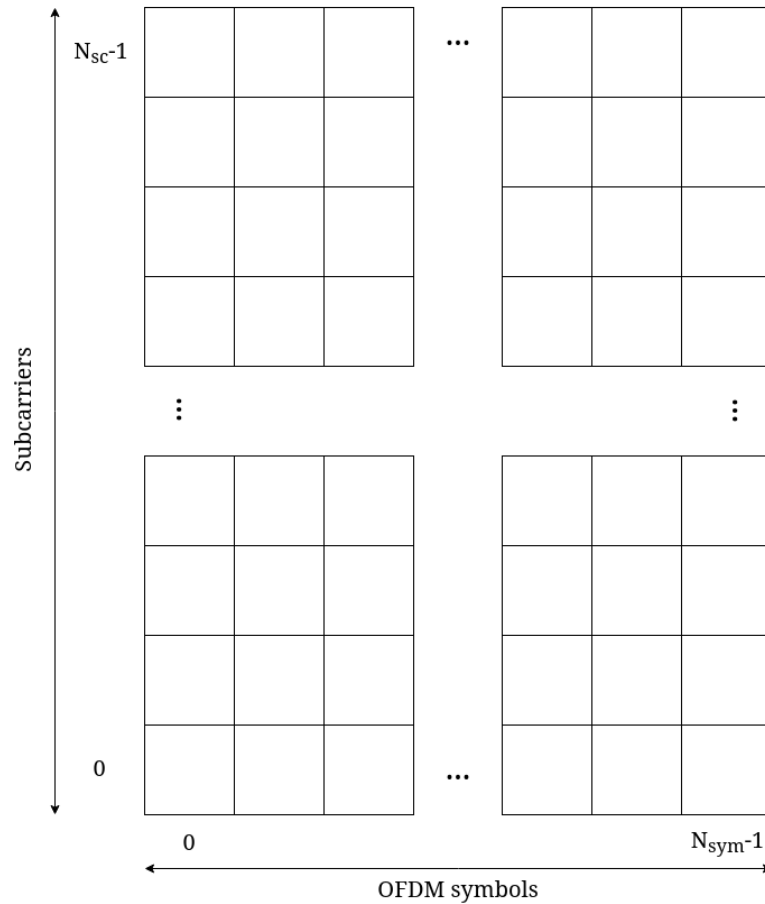
Figure 3.1: OFDM resource grid

3.1 System model

Much like in previous generation long term evolution (LTE) cellular networks, 5G-NR relies on orthogonal frequency division multiplexing (OFDM) in the physical layer (PHY), as specified by 3GPP in the standard [rGPPG20b]. OFDM [Mol12] is a multicarrier transmission scheme, which partitions the entire system bandwith into N_{sc} mutually orthogonal narrowband subcarriers. Due to the orthongonality, the subcarriers only overlap in their zero-crossings in the frequency domain and hence in principle no subcarrier will interfer with any other. The serial input data symbol stream $(S_i)_{i \geq 0}$ is split up into blocks of N_{sc} symbols, which are in turn distributed over the entire bandwidth to modulate the available N_{sc} subcarriers in parallel. An N_{sc}-length symbol block is referred to as an OFDM symbol. This idea of orthogonal subcarriers is conveniently represented by the OFDM resource grid, which is a complex $N_{sc} \times N_{sym}$ matrix, where N_{sym} is the number of consecutive OFDM symbols. The resource grid is shown in figure 3.1.

In 5G-NR a new parameter - the numerology $\mu \in \{0, \ldots, 4\}$ - is introduced. It defines
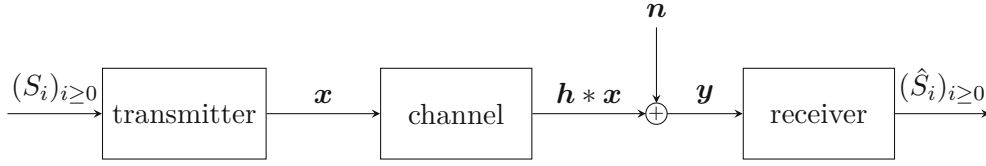
Figure 3.2: Transmission model

the subcarrier spacing $\Delta f_{sc} = 15 * 2^{\mu}$ kHz, the duration $T_{sym} = \frac{1}{\Delta f_{sc}}$ of an OFDM symbol and the number of OFDM symbols $N_{sym} = 14 * 2^{\mu}$ per 1 ms subframe, where 10 subframes form a frame. In LTE, only a single subcarrier spacing of $\Delta f_{sc} = 15$ kHz is defined. Each subframe can be subdivided into a varying number of slots with fixed $N_{sym} = 14$, where the number of slots per subframe depends again on μ. Each position in the resource grid represents a resource block (RB), which is associated with a single and unique subcarrier. A data symbol from the input stream is assigned to a RB in order to modulate the corresponding subcarrier. After the OFDM modulation, the parallel data stream is transformed to the time domain and serialized. The time domain waveform is transmitted through a radio channel with additive noise, before being parallelized again. The received data stream is then transformed back into the frequency domain, where the transmitted symbols can be recovered from the received resource grid by applying a suitable detection method. This transmission scheme is outlined in figure 3.2. Note that in the following sections we focus on SISO transmission in the downlink, since time delay and later position estimates should be computed at the UE in order to minimize latency. Hence, no derivations for multi-antenna transmission schemes are made. Unless noted otherwise, the following models are considered in discrete-time.

3.1.1 Transmitter

The transmitter processes the input data symbol stream $(S_i)_{i \geq 0}$ and packs N_{sc} data symbols to construct the l-th OFDM symbol

$$\boldsymbol{X}_l = [S_{l,0}, \ldots, S_{l,N_{sc}-1}]^T \in \mathbb{C}^{N_{sc} \times 1}, \ l = 0, \ldots, N_{sym} - 1, \tag{3.1}$$

where each data symbol modulates a distinct subcarrier. Note that a data symbol could also be unused ($S_i = 0$) or take on the role of a specialized reference or pilot symbol specified by the standard. This frequency domain symbol vector ist then transformed to the time domain by an inverse discrete fourier transform (DFT^{-1}),

$$x'_{l,n} = \frac{1}{N_{FFT}} \sum_{k=0}^{N_{sc}-1} S_{l,k} e^{j \frac{2\pi nk}{N_{FFT}}}, \ l = 0, \ldots, N_{sym} - 1, \ n = 0, \ldots, N_{FFT} - 1 \tag{3.2}$$

generating the baseband time domain OFDM symbol

$$\boldsymbol{x}'_l = [x_{l,0}, \ldots, x_{l,N_{FFT}-1}]^T \in \mathbb{C}^{N_{FFT}\times 1}. \tag{3.3}$$

The DFT^{-1} operation is efficiently realized by the famous inverse fast fourier transform (FFT^{-1}) algorithm with computational complexity $\mathcal{O}(n \log n)$ - as opposed to $\mathcal{O}(n^2)$ when naively realized as a matrix-vector product. The fast fourier transform (FFT) size N_{FFT} is typically chosen such that it is the smallest power of two which greater is than N_{sc}. If required, the frequency domain vector $\boldsymbol{X}_l$ can be adapted to this size by symmetrically zero-padding it on either end. Hence we can write

$$\boldsymbol{x}'_l = \mathcal{FFT}^{-1}\{\boldsymbol{X}'_l\} \in \mathbb{C}^{N_{FFT}\times 1}, \tag{3.4}$$

where $\boldsymbol{X}'_l$ is the vector $\boldsymbol{X}_l$ zero-padded to length N_{FFT}. The transmitted signal now occupies a bandwidth of $B = N_{sc}\Delta f_{sc}$. The sample rate f_s is governed by the oversampling introduced due to the FFT size N_{FFT} and is given by $f_s = N_{FFT}\Delta f_{sc}$, with sample period $T_s = \frac{1}{f_s}$.

The time domain OFDM symbol $\boldsymbol{x}'_l$ is then prepended by a cyclic prefix with length N_{cp}

$$\boldsymbol{x}^{cp}_l = [x_{l,N_{FFT}-N_{cp}-1}, \ldots, x_{l,N_{FFT}-1}]^T \in \mathbb{C}^{N_{cp}\times 1}, \tag{3.5}$$

by simply duplicating the last N_{cp} samples of $\boldsymbol{x}'_l$. Stacking $\boldsymbol{x}^{cp}_l$ and $\boldsymbol{x}'_l$ yields the full time domain transmit signal

$$\boldsymbol{x}_l = [\boldsymbol{x}^{cp}_l \boldsymbol{x}'_l] = [x_{l,-N_{cp}}, \ldots, x_{l,0}, \ldots, x_{l,N_{FFT}-1}]^T \in \mathbb{C}^{(N_{FFT}+N_{cp})\times 1} \tag{3.6}$$

for the l-th OFDM symbol, as visualized in figure 3.3. This cyclic prefix serves two purposes. On the one hand, it converts the linear convolution of the transmit signal and the channel impulse response (CIR) to a cyclic convolution. This allows for simple frequency domain processing, as the convolution theorem of the discrete fourier transform (DFT) states that a cyclic convolution with the CIR in the time domain is equivalent to a multiplication with the channel frequency response (CFR) in the frequency domain. On the other hand, the cyclic prefix serves as a guard interval between OFDM symbols, limiting the effect of intersymbol interference (ISI). If the maximum excess delay of the channel is not greater than the length of the cyclic prefix, ISI of two consecutive OFDM symbols can be avoided by simply discarding the cyclic prefix at the receiver. The behavior of the cyclic prefix is further elaborated in section 3.1.3.

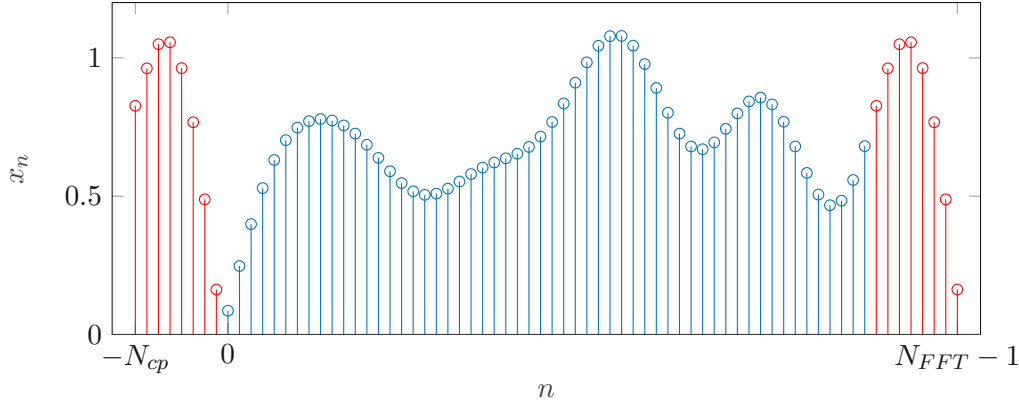Based on the above definitions, we can now define the resource grid for one OFDM slot as

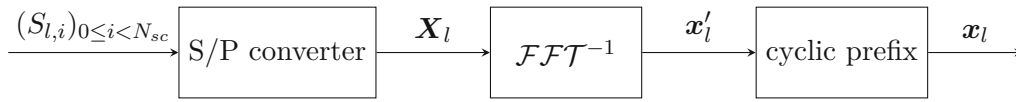Figure 3.3: The values in red are prepended to form the cyclic prefix

Figure 3.4: Transmitter

$$\boldsymbol{X} = [\boldsymbol{X}_0, \ldots, \boldsymbol{X}_{N_{sym}-1}] \in \mathbb{C}^{N_{sc} \times N_{sym}} \tag{3.7}$$

and the corresponding stacked time domain signal vector as

$$\boldsymbol{x} = [\boldsymbol{x}_0 \ldots \boldsymbol{x}_{N_s-1}] = [\boldsymbol{x}_0^{cp}\boldsymbol{x}_0' \ldots \boldsymbol{x}_{N_{sym}-1}^{cp}\boldsymbol{x}_{N_{sym}-1}'] \in \mathbb{C}^{N_{sym}(N_{FFT}+N_{cp}) \times 1}, \tag{3.8}$$

where $N_{sym} = 14$.

Figure 3.4 summarizes the transmission of the l-th OFDM symbol. If the transmitter is to be realized, the time domain digital signal will be passed through a digital-to-analog converter (DAC) and handed over to an radio frequency (RF) chain before transmission. However, these components of the transmitter do not play a role in the following investigations and are hence not further elaborated.

3.1.2 5G positioning reference signal

For the purpose of time delay estimation in the context of positioning, we employ the positioning reference signal (PRS) as defined by the 3GPP standard [rGPPG20b] for 5G-NR. The PRS is composed by a pseudo-random symbol sequence $(r_m)_{m\geq0}$, whose parameters are known both at the transmitter and the receiver and which is given by

$$r_m = \frac{1}{\sqrt{2}}(1 - 2c(2m)) + j\frac{1}{\sqrt{2}}(1 - 2c(2m + 1)), \ m = 0, 1, \ldots, \tag{3.9}$$

where $c(i)$ is the output of a pseudo-random length-31 Gold sequence specified by the standard. The Gold sequence is initialized by a term incorporating information like the number of OFDM symbols per slot, the current slot number and a unique identifier of the transmitter (e.g. the cell ID), yielding a different, pseudo-random PRS at each time slot and for each transmitter. From the definition of the random symbol stream it is visible that it follows the quadrature phase shift keying (QPSK) modulation scheme. The symbols r_m cover the entire bandwidth and are distributed over the resource grid as follows:

$$S_{l,k} = \beta_{PRS} r_m, \ m = 0, 1, \ldots \tag{3.10}$$

$$k = mK_{comb}^{PRS} + \left((k_{offset}^{PRS} + k') \bmod K_{comb}^{PRS}\right) \tag{3.11}$$

$$l = l_{start}^{PRS}, l_{start}^{PRS} + 1, \ldots, l_{start}^{PRS} + L_{PRS} - 1. \tag{3.12}$$

The parameter $L_{PRS} \in \{2, 4, 6, 12\}$ specifies the number of OFDM symbols occupied by the PRS resource in a slot, l_{PRS} is the index of the first OFDM symbol in a slot and β_{PRS} is a power scaling factor. The comb size $K_{comb}^{PRS} \in \{2, 4, 6, 12\}$ specifies the spacing between two PRS symbols in the resource grid, i.e. $K_{comb}^{PRS} = 12$ signifies that 11 subcarriers are left empty between two symbols. Note that $L_{PRS} \equiv 0 \bmod K_{comb}^{PRS}$ must be satisified. k' is the offset at each symbol, resulting from the selected comb size and $k_{offset}^{PRS} \in \{0, 1, \ldots, K_{comb}^{PRS} - 1\}$ is the initial subcarrier offset. More in-depth explanation of the PRS generation process is given in the aforementioned standard and in [MKE+21, dPRLSSG+12]. A typical PRS configuration is visualized in figure 3.5.

Due to the employment of a Gold sequence, the PRS has strong autocorrelation and weak cross-correlation properties, which makes it well-suited to correlation-based time delay estimation at the receiver in presence of multiple simultaneous PRS transmissions originating from different cells [DSM+21]. Multiple mechanisms strive to minimize inter-cell interference, such as different pseudo-random sequences based on the cell ID and a comb structure of the symbols in a PRS resource, with the option of a distinct frequency offset k_{offset}^{PRS} per cell. Furthermore, the standard specifies extensive PRS muting options, where the transmissions of multiple cells can be coordinated and hence hearability of a PRS resource can be increased due to decreased inter-cell interference. Further explanation of the available configuration parameters is given by the documentation in [MATc].
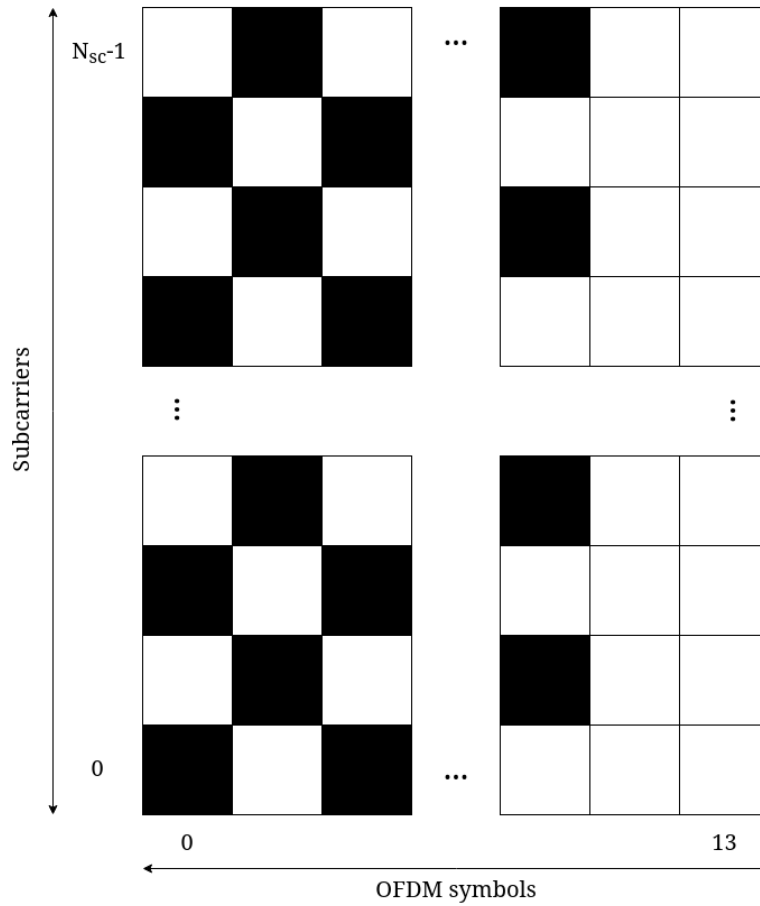
Figure 3.5: PRS slot with $L_{PRS} = 12$, $K_{comb}^{PRS} = 2$ and $k_{offset}^{PRS} = 0$ (black squares denote subcarriers occupied by PRS)

3.1.3 Channel

In this work we consider multipath or frequency-selective channels, which tend to occur in cluttered environments with multiple signal reflectors or scatterers. Such a multipath CIR is typically modelled as a complex lowpass filter in the time domain [LP04]

$$h(t) = \sum_{l=0}^{N_p-1} \alpha_l \delta(t - \tau_l), \tag{3.13}$$

where N_p is the number of propagation paths in the model, $\alpha_l = |\alpha_l|e^{j\theta_l} \in \mathbb{C}$ is the complex path gain with random phase $\theta_l \sim \mathcal{U}(0, 2\pi)$ and $\tau_l \in \mathbb{R}_{\geq 0}$ is the delay of the l-th propagation path. Note that the paths are indexed in accordance with ascending delay duration. Therefore τ_0 corresponds to the delay of the direct path, any non-direct path

19

has a greater delay and thus a greater index. The discrete-time, or sampled, version of the CIR is approximated by a finite impulse response (FIR) filter

$$h_n = \sum_{l=0}^{\tilde{N}_p-1} \tilde{\alpha}_l \delta_{n-\tilde{\tau}_l}, \ n = 0, \ldots, N_h - 1. \tag{3.14}$$

Due to the sampling of the CIR, information about narrow-spaced paths arrivals might be lost if their relative path delays are smaller than the sampling period T_s. In that case, all paths with delays within the interval of the same sample are combined. This is denoted by the altered values $\tilde{N}_p, \tilde{\alpha}_l, \tilde{\tau}_l$, which represent the effect of sampling. We now have $\tilde{N}_p \leq N_p$, as multiple paths might collapse into a single FIR filter tap, $\tilde{\tau}_l \in \mathbb{N}$ since delays are now multiples of the sampling period and $\tilde{\alpha}_l$, which might combine the attenuation of multiple paths. In simulation, the discrete-time CIR is typically implemented as a fractional delay FIR filter [IM08]. The length of the discrete-time CIR is given by the sampled tap delay of the longest path $N_h = \tilde{\tau}_{\tilde{N}_p-1} + 1$. Passing the time domain transmit signal $\boldsymbol{x}$ through a multipath channel modelled by a FIR filter leads to the linear convolution

$$y_n = (\boldsymbol{h} * \boldsymbol{x})_n = \sum_{m=0}^{N_h-1} h_m x_{n-m}, \ n = 0, \ldots, N_{sym}(N_{FFT} + N_{cp}) + N_h - 1. \tag{3.15}$$

We can see that the output value at time n only depends on the N_h previous values of the transmit signal. If the length of the channel N_h is not greater than the length of the cyclic prefix N_{cp}, hence $N_h \leq N_{cp}$ holds, the linear convolution with the l-th OFDM symbol becomes a cyclic convolution, indicated by the operator $\circledast$:

$$y'_{l,n} = (\boldsymbol{h} * [\boldsymbol{x}_l^{cp}\boldsymbol{x}'_l])_n = (\boldsymbol{h} * \boldsymbol{x}_l)_n = \sum_{m=0}^{N_h-1} h_m x_{l,n-m} \tag{3.16}$$

$$= \sum_{m=0}^{N_h-1} h_m x'_{l,(n-m) \bmod N_{FFT}} = (\boldsymbol{h} \circledast \boldsymbol{x}'_l)_n, \ n = 0, \ldots, N_{FFT} - 1. \tag{3.17}$$

This is due to the fact that the cyclic prefix replicates the tail of the OFDM symbol and hence the symbol appears to be periodic with period N_{FFT} to a channel with $N_h \leq N_{cp}$. The cyclic prefix also admits a simple input-output relationship for the l-th OFDM symbol in the frequency domain, given by

$$\boldsymbol{Y}'_l = \boldsymbol{H} \circ \boldsymbol{X}'_l, \text{ with } \boldsymbol{H} = \mathcal{DFT}\{\boldsymbol{h}\}. \tag{3.18}$$

The operator $\circ$ signifies the Schur product and is simply an elementwise multiplication of vectors, resulting from the convolution theorem of the DFT. Moreover, it now becomes clear how the cyclic prefix prevents ISI if $N_h \leq N_{cp}$. In this case, interference due to the channel from the preceeding, $l-1$-th OFDM symbol only affects the cyclic prefix,

$$y_{l,n}^{cp} = (\boldsymbol{h} * [\boldsymbol{x}_{l-1}' \boldsymbol{x}_l^{cp}])_n, \ n = -N_{cp}, \ldots, -1, \tag{3.19}$$

which is discarded at the receiver. The received signal $\boldsymbol{y}$ can, much like the transmit signal x, be viewed as an alternating sequence of cyclic prefix and OFDM symbols:

$$\boldsymbol{y} = [\boldsymbol{y}_0 \ldots \boldsymbol{y}_{N_s-1}] = [\boldsymbol{y}_0^{cp} \boldsymbol{y}_0' \ldots \boldsymbol{y}_{N_s-1}^{cp} \boldsymbol{y}_{N_s-1}'] \in \mathbb{C}^{N_{sym}(N_{FFT}+N_{cp}) \times 1}. \tag{3.20}$$

Another representation [LP04] of the multipath channel is given by the fourier transform of 3.13:

$$H(f) = \sum_{l=0}^{N_p-1} \alpha_l e^{-j2\pi f \tau_l}. \tag{3.21}$$

This CFR can be discretized with respect to the OFDM subcarriers, hence sampled at every subcarrier frequency. This yields a channel coefficient for each subcarrier k, which is given by

$$H_k = \sum_{l=0}^{N_p-1} \alpha_l e^{-j2\pi \Delta f_{sc} k \tau_l}, \ k = 0, \ldots N_{sc} - 1. \tag{3.22}$$

Note how in this representation information about individual, narrow-spaced path delays are preserved in the phase of the channel coefficient, which is why we use this representation as opposed to the model given by 3.14. Combining all channel coefficients H_k into a channel vector $\boldsymbol{H}$ leads to an input-output relationship as in 3.18, while $\boldsymbol{h} = \mathcal{DFT}^{-1}\{\boldsymbol{H}\}$ leads to the relationship 3.15.

Since the goal of this thesis is to estimate a position vector via radio signals, we need to incorporate range information in the propagtion channel. Given 2D or 3D coordinate vectors $\boldsymbol{r}_{tx}$ and $\boldsymbol{r}_{rx}$ of the transmitter and receiver respectively, the propagation delay due to the distance between both amounts to

$$\tau_r = \|\boldsymbol{r}_{tx} - \boldsymbol{r}_{rx}\|_2 / c_0, \ \tau_r \in \mathbb{R}_{\geq 0}, \tag{3.23}$$

where c_0 corresponds to the propagation speed. As we are dealing with sampled signals, this delay is further split up into

$$\tau_r^s = \lfloor \tau_r/T_s \rfloor, \ \tau_r^{res} = \tau_r - \tau_r^s T_s. \tag{3.24}$$

The residual fractional delay is modelled by applying a phase shift, resulting in $\boldsymbol{h} = \mathcal{FFT}^{-1}\{\boldsymbol{H} \circ [1, e^{-j2\pi\tau_r^{res}/N_{FFT}}, \ldots, e^{-j2\pi(N_{FFT}-1)\tau_r^{res}/N_{FFT}}]^T\}$, while τ_r^s is realized by delaying the received signal by τ_r^s samples.

In addition to the propagation channel, we include additive white gaussian noise (AWGN). This serves to model thermal noise at the receiver. AWGN is parameterized by the mean noise power σ_n^2, hence we obtain the time domain noise vector as

$$\boldsymbol{n} \sim \sqrt{\frac{\sigma_n^2}{2}}\left(\mathcal{N}\left(\boldsymbol{0}, \boldsymbol{I}\right) + j\mathcal{N}\left(\boldsymbol{0}, \boldsymbol{I}\right)\right) \in \mathbb{C}^{N_{sym}(N_{FFT}+N_{cp})\times 1} \tag{3.25}$$

and the full time domain signal at the receiver input as

$$\boldsymbol{y} = (\boldsymbol{h} * \boldsymbol{x}) + \boldsymbol{n}. \tag{3.26}$$

In the frequency domain the relationship is similar. The noise vector is given by

$$\boldsymbol{N}_l \sim N_{FFT}\sqrt{\frac{\sigma_n^2}{2}}\left(\mathcal{N}\left(\boldsymbol{0}, \boldsymbol{I}\right) + j\mathcal{N}\left(\boldsymbol{0}, \boldsymbol{I}\right)\right) \in \mathbb{C}^{N_{FFT}\times 1} \tag{3.27}$$

and hence the l-th received OFDM symbol is given as

$$\boldsymbol{Y}_l' = \boldsymbol{H} \circ \boldsymbol{X}_l' + \boldsymbol{N}_l. \tag{3.28}$$

Note the scaling of the noise power in the frequency domain due to Parseval's theorem.

3.1.4 Receiver

The serial input stream at the receiver is given by

$$\boldsymbol{y} = [\boldsymbol{y}_0 \ldots \boldsymbol{y}_{N_s-1}] = [\boldsymbol{y}_0^{cp}\boldsymbol{y}_0' \ldots \boldsymbol{y}_{N_{sym}-1}^{cp}\boldsymbol{y}_{N_{sym}-1}'] \in \mathbb{C}^{N_{sym}(N_{FFT}+N_{cp})\times 1}, \tag{3.29}$$
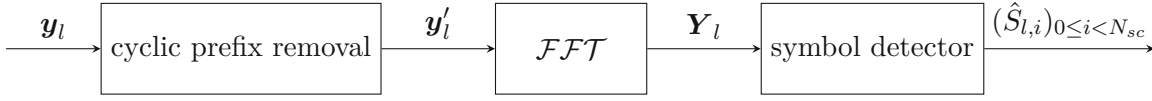
Figure 3.6: Receiver

where $\boldsymbol{y}$ is distorted by the channel $\boldsymbol{h}$ and corrupted by the noise $\boldsymbol{n}$, as explained in the previous sections. The receiver removes the cyclic prefix, resulting in the vector

$$\boldsymbol{y}' = [\boldsymbol{y}'_0 \ldots \boldsymbol{y}'_{N_{sym}-1}] \in \mathbb{C}^{N_{sym}(N_{FFT}) \times 1}. \tag{3.30}$$

In a next step, the receiver parallelizes the input stream by combining N_{FFT} samples into the l-th OFDM symbol $\boldsymbol{y}'_l \in \mathbb{C}^{N_{FFT} \times 1}$, which serves as a basis for further processing. Subsequently, the receiver demodulates the received OFDM symbol by performing an FFT, yielding the corresponding frequency domain OFDM symbol

$$\boldsymbol{Y}_l = \mathcal{FFT}\{\boldsymbol{y}'_l\} \in \mathbb{C}^{N_{FFT} \times 1}. \tag{3.31}$$

By combining the received OFDM symbols and truncating the FFT overhead, we obtain the received resource grid

$$\boldsymbol{Y} = [\boldsymbol{Y}_0, \ldots, \boldsymbol{Y}_{N_{sym}-1}] \in \mathbb{C}^{N_{sc} \times N_{sym}}. \tag{3.32}$$

If the received signal should be subject to further processing, it will be passed to a symbol detection algorithm. This however is not of relevance to the investigations in this thesis and hence will not be further elaborated on. Figure 3.6 outlines the reception of the l-th OFDM symbol.

3.2 Time delay estimation in harsh environments

The goal of this thesis is to investigate the positioning capabilities of 5G-NR cellular networks, with an emphasis on vehicular applications. Hence it is necessary to study the radio signal propagation environments arising in different vehicular scenarios. On a coarse scale, vehicular scenarios can be split into rural and (sub-)urban settings. In the former, we would expect that LOS links dominate and the amount of reflected paths is limited - with the notable exception of wooded or mountainous areas. The latter, (sub-)urban setting, is characterized by many cluttering objects, mainly buildings of varying heights. In such an urban scenario, we anticipate a large share of NLOS links with a more frequent
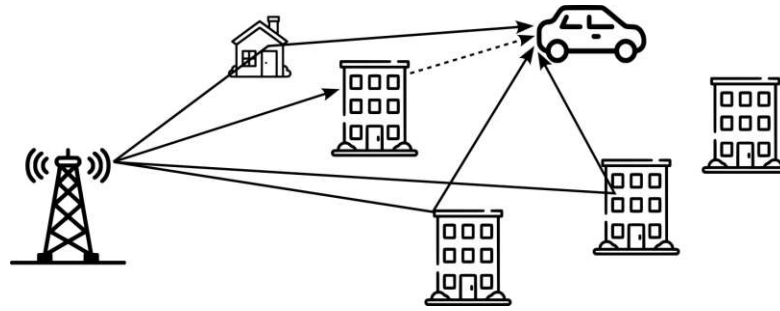
Figure 3.7: Typical multipath propagation with blocked LOS path in an urban setting
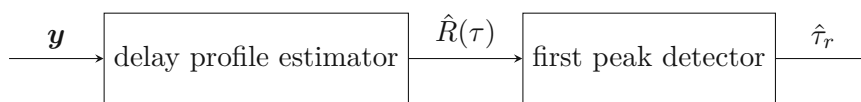

Figure 3.8: Two-step time delay estimation procedure

switch between LOS and NLOS links due to the successive appearence of buildings and empty gaps between them. Furthermore, we expect many reflectors and scatterers in an urban setting. This type of propagation is visualized in figure 3.7.

Dense multipath propagation channels like this can be modelled by the methods outlined in section 3.1.3. In this work, we want to focus on scenarios of the latter type, since traditional positioning techniques based on GNSS typically suffer from performance degradation in urban situations [WGZ13, KKSM17], as opposed to the rural, open-field-type scenario. Time delay estimation for NLOS links poses a special challenge - mainly because the direct path may be heavily attenuated due to blockages. This leads to a situation where the direct path might not necessarily be the most powerful path or even might not be detectable at all. In this case, the strategy for estimating the time delay by detecting the strongest path, which is the maximum likelihood (ML)-optimum estimator for the AWGN channel [dPRLSSG$^+$12], obviously fails if high ranging accuracy is desired. Hence, in the following sections we will present and investigate methods for improved time delay estimation in NLOS multipath channels. We split this task into two sub-tasks, yielding the two-stage system shown in figure 3.8. At first, a delay profile estimate $\hat{R}(\tau)$ of the channel is required, which can be obtained from the received signal $\boldsymbol{y}$. An appropriate estimator would generate peaks close to the arrival times of the multipath components in such a delay profile. In a second step, a suitable detector is tasked with locating the first peak in the delay profile, were we assume that it results from the direct path. The delay of this detected peak amounts to the estimated propagation delay $\hat{\tau}_r$. The delay profile estimation methods studied in this thesis are presented in section 3.3, while the delay peak detection methods are outlined in 3.4.
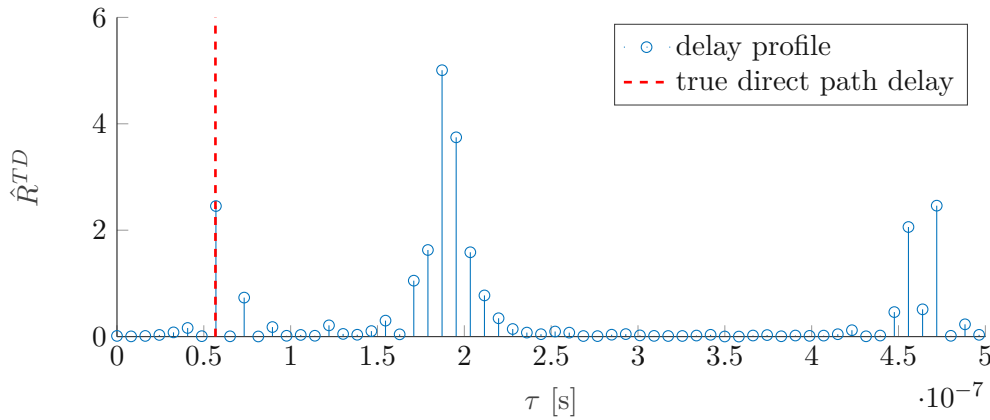
Figure 3.9: Typical time domain correlation delay profile

3.3 Delay profile estimation methods

3.3.1 Time domain correlation

Estimating a delay profile for delay measurement purposes by time domain cross-correlation can be considered the standard, or textbook approach [KC76, ZB11]. It serves as the basis for the ML-optimum delay estimator in the AWGN channel. The delay profile is obtained by correlating the received signal $\boldsymbol{y}$ with the time domain PRS $\boldsymbol{x}$ emitted by a specific BS, which must be known at the receiver:

$$\hat{R}_\tau^{TD} = |\sum_{l=0}^{N_{sym}-1} \sum_{n=0}^{N_{FFT}-1} y_{l,n+\tau}^* x_{l,n}|^2, \ \tau = 0,\ldots,\tau_{max}. \tag{3.33}$$

A typical delay profile obtained by time domain correlation is shown in figure 3.9. Advantages of this method are that it can directly operate on the received time domain signal and the relatively low complexity. Disadvantages are that the resolution of the method strongly depends on the signal bandwidth and that it is not capable of seperating closely-spaced multipath components. The residual delay error $\epsilon(\tau)$ of individual paths due to the limited resolution can be modelled by the variance of a uniform distribution over the length of one sample [Men13] and is given by

$$\epsilon(\tau) = \frac{1}{\sqrt{12}} \frac{1}{N_{FFT} f_{sc}}. \tag{3.34}$$

3.3.2 Frequency domain correlation

Another approach for estimating a delay profile is to correlate the received OFDM symbol $\boldsymbol{Y}_l$ and the known reference OFDM symbol $\boldsymbol{X}_l$ in the frequency domain [Men13]:
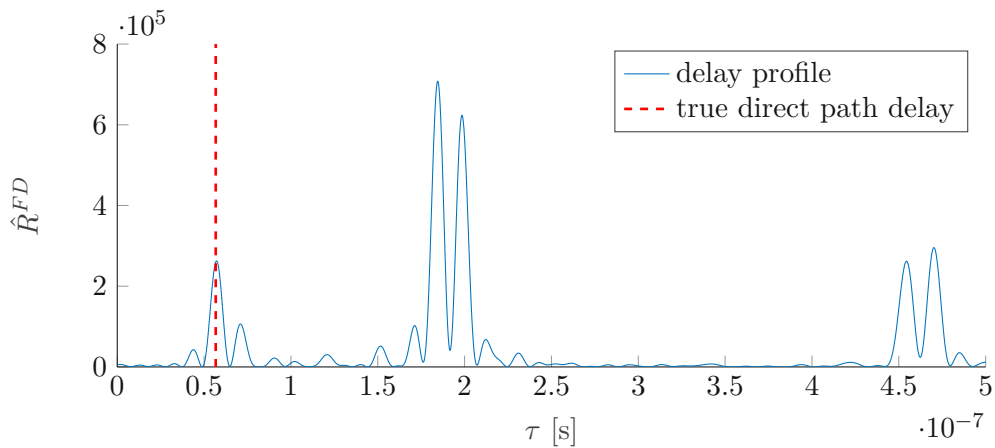
Figure 3.10: Typical frequency domain correlation delay profile

$$\hat{R}(\tau) = |\sum_{k=0}^{N_{sc}-1} e^{-j2\pi(k-\lfloor(N_{sc}-1)/2\rfloor)F_{sc}\tau} \; Y_{l,k}^* X_{l,k}|^2, \; \tau \in [0, \tau_{max}]. \tag{3.35}$$

An example is shown in figure 3.10. Advantages of this method are that it allows for interpolation in between samples and therefore in theory offers increased delay resolution. This is reflected by the fact that the delay τ is now a real number in an interval. The main disadvantages are that the method requires the demodulation of the received signal and the increased computational complexity due to the interpolation. Furthermore, it is not able to seperate closely-spaced multipath components.

3.3.3   MUSIC

Recall the CFR given by 3.36. If the roles of time delay τ and frequency f are switched, we obtain

$$H(\tau) = \sum_{l=0}^{N_p-1} \alpha_l e^{-j2\pi f_l \tau}. \tag{3.36}$$

We observe that this formula is equivalent to the harmonic signal model, which implies that spectral estimation algorithms tailored to the harmonic signal model can be employed for estimating a delay profile from a multipath CFR [LP04]. The multiple signal classification (MUSIC) algorithm [Sch86] is a well-known superresolution method for estimating frequencies in a harmonic signal model, often with the goal of obtaining angles of arrival from signals inbound to an antenna array. Many authors have studied the applicability of MUSIC to the estimation of delay profiles in multipath radio channels

[LP04, ZYLS07, GSPL04, DZW$^+$20], with promising results. In this thesis, we closely follow the ideas presented in [LP04], where the authors proposed MUSIC delay estimation method that can be applied to 5G-NR.

MUSIC requires an estimate $\hat{\boldsymbol{H}}$ of the channel as an input, which can be obtained by employing the deconvolution method in OFDM systems [ZYLS07]:

$$\hat{\boldsymbol{H}} = \boldsymbol{Y} \circ \frac{1}{\boldsymbol{X}} = \boldsymbol{H} + \boldsymbol{N} \circ \frac{1}{\boldsymbol{X}} = \boldsymbol{H} + \boldsymbol{W} \in \mathbb{C}^{N_{sc} \times 1}. \tag{3.37}$$

Recall the elementwise vector multiplication denoted by the operator $\circ$. The received signal is simply divided by the reference signal symbols in the frequency domain, which leads to an estimate of the channel coefficients at each subcarrier. Note that as a result of the deconvolution operation, the white gaussian noise $\boldsymbol{N}$ now becomes a colored noise vector $\boldsymbol{W}$. The main concept behind MUSIC is that the algebraic space spanned by the autocorrelation matrix $\boldsymbol{R}_{\hat{H}\hat{H}}$ of the estimated channel can be seperated in channel and noise subspaces $\mathcal{H}$ and $\mathcal{W}$ by computing the eigendecomposition of $\boldsymbol{R}_{\hat{H}\hat{H}}$:

$$\boldsymbol{R}_{\hat{H}\hat{H}} = \mathcal{E}\{\hat{\boldsymbol{H}}\hat{\boldsymbol{H}}^H\} = \boldsymbol{R}_{HH} + \boldsymbol{R}_{WW} \in \mathbb{C}^{N_{sc} \times N_{sc}}, \tag{3.38}$$

$$\boldsymbol{R}_{\hat{H}\hat{H}} = \boldsymbol{U}\boldsymbol{\Lambda}\boldsymbol{U}^H = \boldsymbol{U}_{\mathcal{H}}\boldsymbol{\Lambda}_{\mathcal{H}}\boldsymbol{U}_{\mathcal{H}}^H + \boldsymbol{U}_{\mathcal{W}}\boldsymbol{\Lambda}_{\mathcal{W}}\boldsymbol{U}_{\mathcal{W}}^H. \tag{3.39}$$

$\mathcal{E}\{\cdot\}$ denotes the linear expectation operation, the matrix $\boldsymbol{\Lambda}$ is a diagonal matrix with the eigenvalues λ_i, $i = 0, \ldots, N_{sc} - 1$ of $\boldsymbol{R}_{\hat{H}\hat{H}}$ as the diagonal elements and the matrix $\boldsymbol{U}$ contains the corresponding eigenvectors $\boldsymbol{u}_i$, $0 < i < N_{sc} - 1$. We further decompose $\boldsymbol{R}_{HH} = \boldsymbol{V}\boldsymbol{A}\boldsymbol{V}^H$, with

$$\boldsymbol{V} = [\boldsymbol{v}(\tau_0), \ldots, \boldsymbol{v}(\tau_{N_p-1})], \tag{3.40}$$

$$\boldsymbol{v}(\tau_l) = [1, e^{-j2\pi\Delta f_{sc}\tau_l}, \ldots, e^{-j2\pi(N_{sc}-1)\Delta f_{sc}\tau_l}]^T, \tag{3.41}$$

$$\boldsymbol{A} = \mathcal{E}\{\boldsymbol{a}\boldsymbol{a}^H\}, \ \boldsymbol{a} = [\alpha_0, \ldots, \alpha_{N_p-1}]^T. \tag{3.42}$$

It can be shown that the matrix rank of $\boldsymbol{V}\boldsymbol{A}\boldsymbol{V}^H$ is N_p and that the smallest $N_{sc} - N_p$ eigenvalues correspond to the noise autocorrelation $\boldsymbol{R}_{WW}$. Hence, by sorting the eigenvalues of $\boldsymbol{R}_{\hat{H}\hat{H}}$ in an descending order, we can seperate the N_{sc}-dimensional space containing $\hat{\boldsymbol{H}}$ into the orthogonal channel and noise subspaces $\mathcal{H}$ and $\mathcal{W}$ as the N_p largest eigenvalues and their corresponding eigenvectors span $\mathcal{H}$, while the eigenvectors corresponding to the remaining $N_{sc} - N_p$ smallest eigenvalues span $\mathcal{W}$. The matrix projecting into the noise subspace is therefore given by $\boldsymbol{P}_{\mathcal{W}} = \boldsymbol{U}_{\mathcal{W}}(\boldsymbol{U}_{\mathcal{W}}^H\boldsymbol{U}_{\mathcal{W}})^{-1}\boldsymbol{U}_{\mathcal{W}}^H = \boldsymbol{U}_{\mathcal{W}}\boldsymbol{U}_{\mathcal{W}}^H$ and due to the orthogonality of $\mathcal{H}$ and $\mathcal{W}$ it holds that $\boldsymbol{P}_{\mathcal{W}}\boldsymbol{v}(\tau_l) = 0$. The MUSIC pseudospectrum, which in this context can be interpreted as a delay profile, is now given by
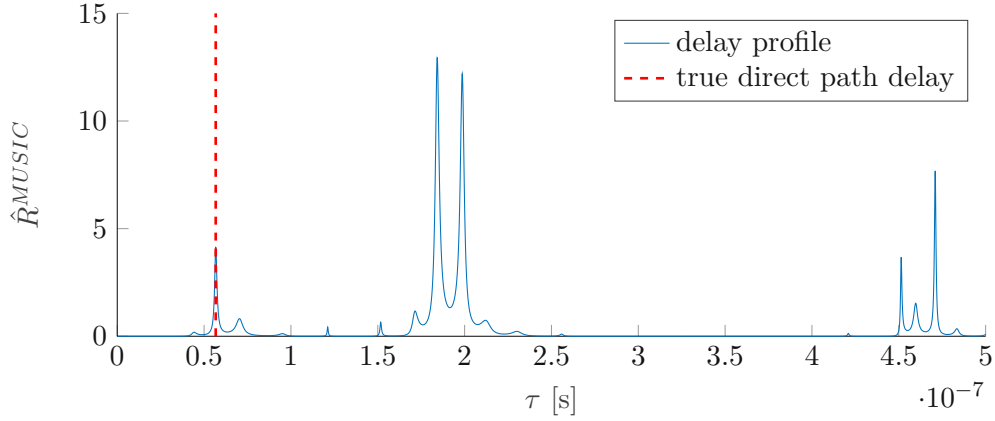
27

Figure 3.11: Typical MUSIC delay profile

$$\hat{R}^{MUSIC}(\tau) = \frac{1}{||\boldsymbol{P}_{\mathcal{W}}\boldsymbol{v}(\tau)||^2} = \frac{1}{||\boldsymbol{U}_{\mathcal{W}}^H\boldsymbol{v}(\tau)||^2} = \frac{1}{\sum_{i=N_p}^{N_{sc}-1}|\boldsymbol{u}_i^H\boldsymbol{v}(\tau)|^2}, \ \tau \in [0, \tau_{max}]. \quad (3.43)$$

The local maxima of this function are located at the estimated multipath delays, as visualized by the example in figure 3.11.

Two issues arise in the practical implementation of the MUSIC method: First, the autocorrelation matrix $\boldsymbol{R}_{\hat{H}\hat{H}} = \mathcal{E}\{\hat{\boldsymbol{H}}\hat{\boldsymbol{H}}^H\}$ cannot be computed exactly and hence must be estimated from a finite dataset. Second, the parameter N_p is unknown and must be estimated as well. The autocorrelation matrix $\boldsymbol{R}_{\hat{H}\hat{H}}$ can be estimated from a single channel measurement $\hat{\boldsymbol{H}}$ in the following way:

$$\hat{\boldsymbol{R}}_{\hat{H}\hat{H}} = \frac{1}{M}\sum_{k=0}^{M-1}\hat{\boldsymbol{H}}_k\hat{\boldsymbol{H}}_k^H, \ \hat{\boldsymbol{H}}_k = [\hat{H}_k, \ldots, \hat{H}_{k+L-1}]^T, \ M = N_{sc} - L + 1. \quad (3.44)$$

Different values for L have been studied in the literature, in this thesis we set $L = \frac{2N_{sc}}{3}$. The estimate of the autocorrelation matrix can be further refined by applying forward-backward smoothing

$$\hat{\boldsymbol{R}}_{\hat{H}\hat{H}}^{FB} = \frac{1}{2}(\hat{\boldsymbol{R}}_{\hat{H}\hat{H}} + \boldsymbol{J}\hat{\boldsymbol{R}}_{\hat{H}\hat{H}}\boldsymbol{J}) \in \mathbb{C}^{L\times L}, \quad (3.45)$$

where the exchange matrix $\boldsymbol{J} \in \mathbb{N}^{L\times L}$ is zero except for the antidiagonal, which is filled with ones. The number of multipath components N_p present in a radio channel realization

can be estimated by employing the minimum descriptive length (MDL) criterion [VT04]. First, a cost function

$$C(\Theta) = M(L - \Theta)\ln\left[\frac{\frac{1}{L-\Theta}\sum_{i=\Theta+1}^{L}\lambda_{i-1}}{\left[\prod_{i=\Theta+1}^{L}\lambda_{i-1}\right]^{\frac{1}{L-\Theta}}}\right]\tag{3.46}$$

is computed, then the estimated number of multipath components is obtained by

$$\hat{N}_p = \arg\min_{\Theta}\left\{C(\Theta) + \frac{1}{2}(\Theta(2L - \Theta) + 1)\ln M\right\}, \Theta = 1, \dots, L.\tag{3.47}$$

There are many further possibilities for refining delay profile estimation with the MUSIC technique, which are however not in the scope of this thesis.

Advantages of this method include the ability to seperate closely-spaced multipath components, the superresolution of the delay profile and an increased robustness against noise due to the seperation of the signal and noise subspaces. Disadvantages include the required demodulation of the received signal and the high computational complexity resulting from the costly eigendecomposition of the autocorrelation matrix and the interpolation of the pseudospectrum. The required a-priori information about the number of multipath components N_p can be considered as an additional drawback.

3.4 Delay peak detection methods

3.4.1 Maximum peak detector

In the AWGN channel, the ML-optimum strategy for estimating the propagation delay $\hat{\tau}_r$ of a reference signal is simply to find the delay of the single time domain correlation peak [dPRLSSG$^+$12]. We extend this method to obtain the estimated delay from an arbitrary delay profile $\hat{R}(\tau)$:

$$\hat{\tau}_r^{MP} = \arg\max_{\tau}\hat{R}(\tau).\tag{3.48}$$

As elaborated in section 3.2 and visualized in figure 3.12, this method is not well-suited for the task of finding the peak due to the direct path in NLOS multipath channels, therefore it is mainly used as a baseline for comparison with the more sophisticated method presented below.
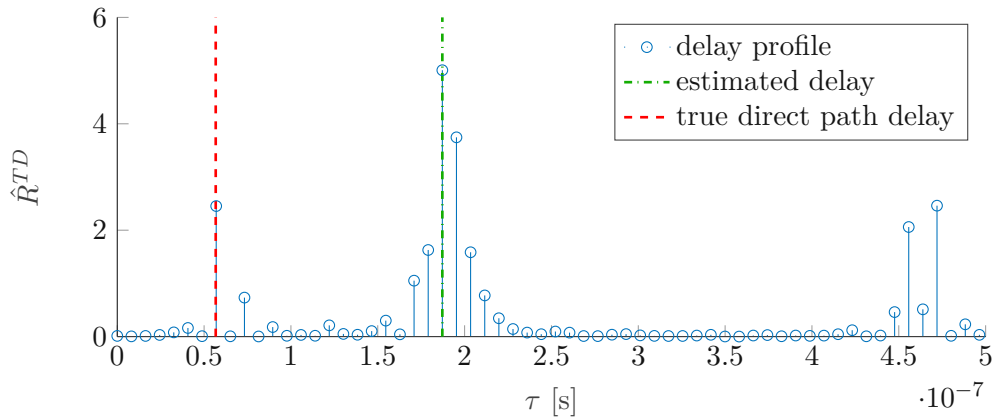
Figure 3.12: Delay estimation in an NLOS channel with the maximum peak detector

3.4.2 Adaptive threshold detector

One approach for detecting the first peak of a delay profile is to define a threshold that adapts to the level of the noise floor present in a certain radio link. For this method, we closely follow the ideas from [XHZD16]. In a first step, a signal arrival region needs to be determined such that the data outside of this region can be used for estimating the level of the noise floor. For this purpose, a moving sum over the delay profile with a window size matched to the length of the cyclic prefix N_{cp} is computed:

$$\hat{R}_{win,\tau} = \sum_{t=\tau}^{\tau+N_{cp}-1} \hat{R}_\tau, \ \tau = 0, \ldots, \tau_{max} - N_{cp} - 1. \tag{3.49}$$

For the superresolution delay profiles, the size of the window must be adapted to account for the interpolation steps. The signal is assumed to having arrived in the interval

$$\tau_{start} \leq \tau \leq \tau_{start} + N_{cp} - 1 \text{ s.t. } \tau_{start} = \arg\max_\tau \hat{R}_{win,\tau}, \tag{3.50}$$

where the moving sum achieves the maximum value. In a next step, the level of the noise floor n_f is determined by averaging the delay profile values outside of the determined signal arrival region. This serves to avoid a possible bias of the noise floor introduced by delay profile peaks. Furthermore, the value of the maximum delay profile peak

$$\hat{R}_{max} = \max_{\tau_{start} \leq \tau \leq \tau_{start} + N_{cp}-1} \hat{R}_\tau \tag{3.51}$$
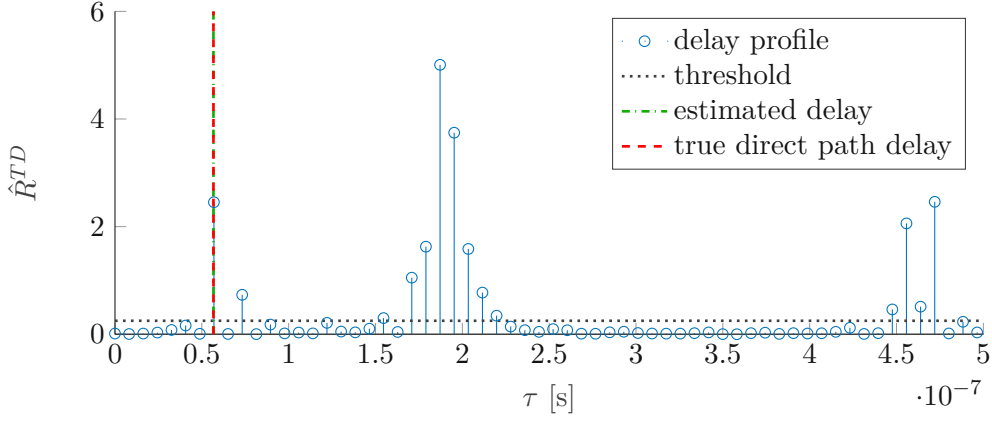
Figure 3.13: Delay estimation in an NLOS channel with the adaptive threshold detector

is determined within the signal arrival region. In a final step, it is now possible to define a threshold based on these parameters:

$$\Theta(n_f, \hat{R}_{max}) = \alpha(\beta \hat{R}_{max} + (1 - \beta)n_f), \ \beta \in [0, 1]. \tag{3.52}$$

In this thesis we set $\alpha = 1$, $\beta = 0.03$, which were found to be values yielding robust and consistent results for multiple channel models. The incorporation of the maximum peak value serves the purpose of raising the threshold in high signal-to-noise ratio (SNR) situations, in order to avoid detecting correlation side lobe peaks. The propagation delay of the first detected path can now be estimated as

$$\hat{\tau}_r^{AT} = \min_{\tau_{start} \leq \tau \leq \tau_{start}+N_{cp}-1} \tau << \ \text{s.t.} \ \hat{R}_\tau \geq \Theta(n_f, \hat{R}_{max}). \tag{3.53}$$

Figure 3.13 visualizes the behavior of this detection method.

For the superresolution algorithms, we have to impose the additional constraint that the first detected path must be at a local maximum of the delay profile.

Advantages of the method are the ability to detect the first peak in a delay profile, while still keeping the computational cost relatively low. The main disadvantage is the necessity for parameter tuning in the threshold definition, which proves to be a challenging task if overfitting to a specific channel model should be avoided.

3.5   Simulations

3.5.1   Channel models

In all simulations done for this thesis, we make use of the stochastic tapped delay line (TDL) channel models specified by the 3GPP standard [rGPPG18]. The channel models are defined by taps at normalized time delays $\boldsymbol{\tau}_{norm}$ and their corresponding average tap powers $\boldsymbol{\rho}$. The NLOS channel taps follow a Rayleigh distribution, while LOS channel taps are Rice-distributed. The Rician first tap has the K-factor $K = 10 \log_{10} \frac{A^2}{\rho_0}$ as an additional parameter, where A^2 refers to the mean power of the direct path. The normalized tap delays must be scaled to the desired delay spread DS, which yields the tap delays $\boldsymbol{\tau} = DS\boldsymbol{\tau}_{norm}$. Realizations of the channel models can be obtained by sampling from a complex gaussian distribution [FE08]. In the NLOS case, the tap coefficients $\boldsymbol{\alpha}$ are generated as follows:

$$\boldsymbol{\alpha} \sim \sqrt{\frac{\boldsymbol{\rho}}{2}}(\boldsymbol{\mathcal{N}}(\boldsymbol{0}, \boldsymbol{I}) + j\boldsymbol{\mathcal{N}}(\boldsymbol{0}, \boldsymbol{I})). \tag{3.54}$$

$\mathcal{N}(\mu, \sigma^2)$ signifies the normal distribution with mean and variance parameters. In case of LOS channel models, the first tap coefficient follows a different distribution:

$$\alpha_0 \sim A + \sqrt{\frac{\rho_0}{2}}(\mathcal{N}(0, 1) + j\mathcal{N}(0, 1)). \tag{3.55}$$

The tap coefficients are normalized such that the channel has unit power and the final values $\boldsymbol{\tau}$ and $\boldsymbol{\alpha}$ are then inserted into the model 3.22 to obtain a discrete-time CFR. The standard specifies the three NLOS channel models TDL-A, TDL-B and TDL-C, with their average-power-delay-profiles shown in figure 3.14. Further, the two LOS channel models TDL-D and TDL-E are specified in the standard, with their average-power-delay-profiles shown in figure 3.14. Note that for the purpose of visualization, the NLOS channel models have been truncated and hence not all taps are shown in the figures. For the simulations, it is assumed that the channel remains constant for the time period of one slot.

3.5.2   Setup

In order to evaluate the ranging accuracy of the algorithms introduced in the sections above, we consider a simple scenario with one receiver and one transmitter. The PRS is passed through channel filters generated from the standard-compliant channel models shown in section 3.5.1 and a random propagation delay sampled from a uniform distribution. Furthermore, we include AWGN and set the noise power such that the SNR values required for the SNR sweep are achieved, according to the definition $SNR = P_{\boldsymbol{x}}/\sigma_n^2$
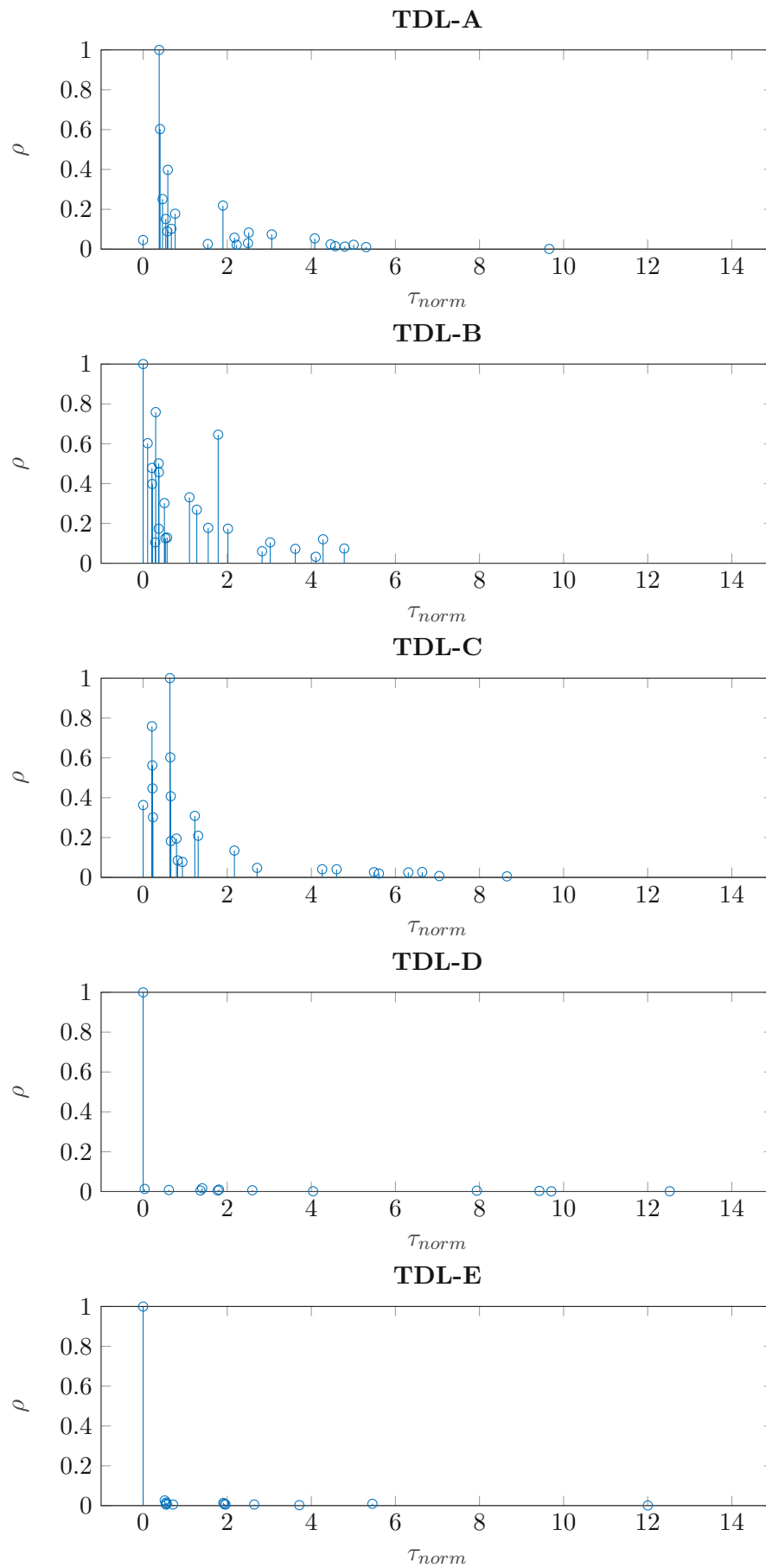
Figure 3.14: 3GPP channel models

33

Name	Value
Monte Carlo repetitions	$N_{mc} = 400$
Transmit bandwidth	$B \in \{20, 50, 100\}$ MHz
Number of subcarriers	$N_{sc} \in \{612, 1596, 3276\}$
FFT size	$N_{FFT} \in \{1024, 2048, 4096\}$
Cyclic prefix length	$N_{cp} \in \{72, 144, 288\}$
Subcarrier spacing	$\Delta f_{sc} = 30$ kHz
Numerology	$\mu = 1$
PRS symbols per slot	$L_{PRS} = 12$
PRS comb size	$K_{comb}^{PRS} = 2$
Channel model	TDL-A - TDL-E
Delay spread	$DS \in \{65, 129, 634\}$ ns
SNR	$SNR \in [-30, 20]$ dB

Table 3.1: Simulation parameters

with $P_{\boldsymbol{x}} = \frac{1}{N} \sum_{n=0}^{N-1} |x_n|^2$. Note that the channel filter can be neglected in this definition due to it being normalized to unit power. Since the time delay estimation algorithms are to be used in a positioning application, we consider the range root mean squared error (RMSE) as performance metric in the simulations. It is defined as

$$RMSE_r = c_0 RMSE_{\tau_r} = c_0 \sqrt{\mathcal{E}\{(\tau_r - \hat{\tau}_r)^2\}}, \qquad (3.56)$$

where the expectation operation is approximated by computing the sample means of N_{mc} Monte Carlo simulation repetitions with different channel, range and noise realizations. Range and delay RMSE are related via the signal propagation speed constant c_0. For evaluating the performance in different scenarios, the simulations are conducted with all TDL channel models listed in section 3.5.1, with different delay spread DS for the channel models and with different bandwidths B. Recall that the bandwidth is configured by the number of subcarriers N_{sc}, which in turn affects the FFT size N_{FFT} and the cylic prefix length N_{cp}. Furthermore, for each simulation repetition one slot with 14 OFDM symbols is transmitted. The delay spread values are suggested by the Urban Microcell (UMi) scenario defined in the standard [rGPPG18]. MATLAB was used for implementing the algorithms and the simulation environment, where features of the 5G toolbox [MATa] were used for standard-compliant signal transmission. The full list of simulation parameters can be found in table 3.1. Note that for symplicity purposes we assume perfect synchronization between receiver and transmitter - this assumption will however be dropped in the next chapters when performing TDOA position estimation.
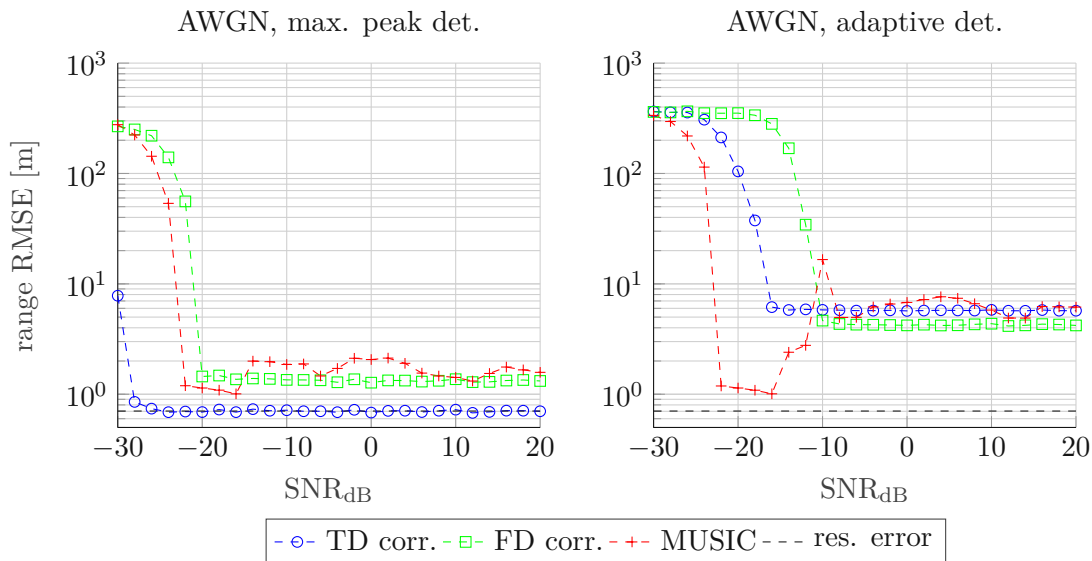
Figure 3.15: Ranging performance comparison for different delay profiles in the AWGN channel, $B = 100$ MHz, $DS = 129$ ns

3.5.3 Results

First, we investigate how the algorithms behave in the AWGN channel. The simulation results for this setting are visualized in figure 3.15. It immediately becomes clear that the combination of the time domain correlation delay profile and maximum peak detector yields the best result with the most accurate estimates, as it represents the ML-optimum estimator in the AWGN channel. Notice also, how the ranging error saturates at the residual error due to the bandwitch, as given by equation 3.34. Frequency domain correlation and MUSIC delay profiles perform slightly worse than that when combined with the maximum peak detector, as they are not ML-optimum. Employing the adaptive threshold first peak detector shows decreased ranging accuracy as compared to the maximum peak detector for all three types of delay profiles. This is due to the fact that in high SNR cases the threshold will be so low that correlation side lobes of the delay peak are wrongly detected as first paths. The situation is even more extreme when looking at the MUSIC curve, where the ranging error curve at first approaches the residual error, but then even rises again for higher SNR due to the threshold dropping to low.

Looking at the simulation results for the NLOS channels depicted in figure 3.16 immeadiately reveals the superiority of the adaptive threshold first peak detector over the maximum peak detector in these situations. While the maximum peak detector yields similar ranging results for all three NLOS channel models (we only show the results for TDL-C since the results for TDL-A and TDL-B were similar), the adaptive threshold detector increases the ranging accuracy by almost one order of magnitude - of course depending on the delay profile estimation method and the channel model. In terms of delay profiles, we observe that with the MUSIC algorithm the ranging error already
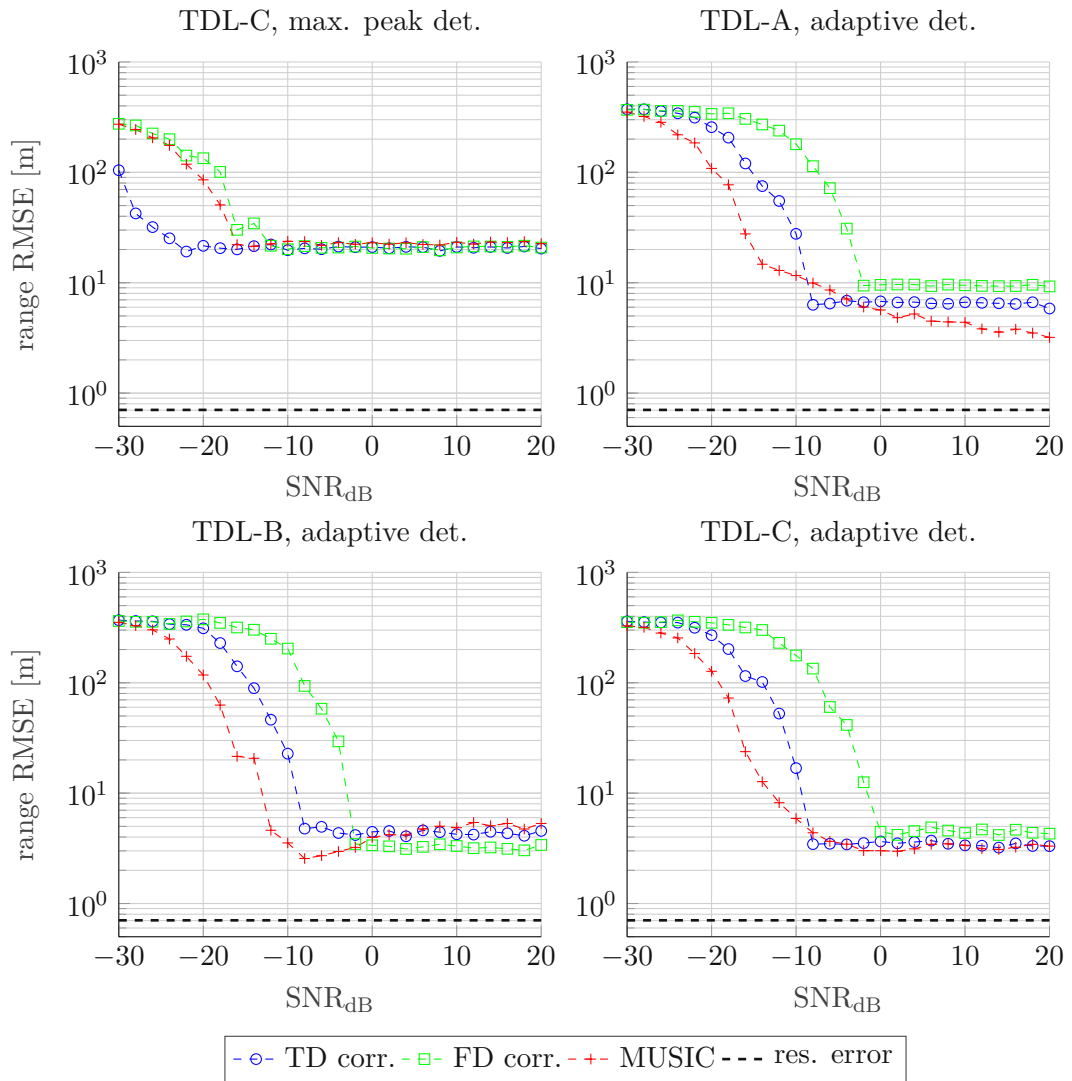
Figure 3.16: Ranging performance comparison for different delay profiles in NLOS channels, $B = 100$ MHz, $DS = 129$ ns
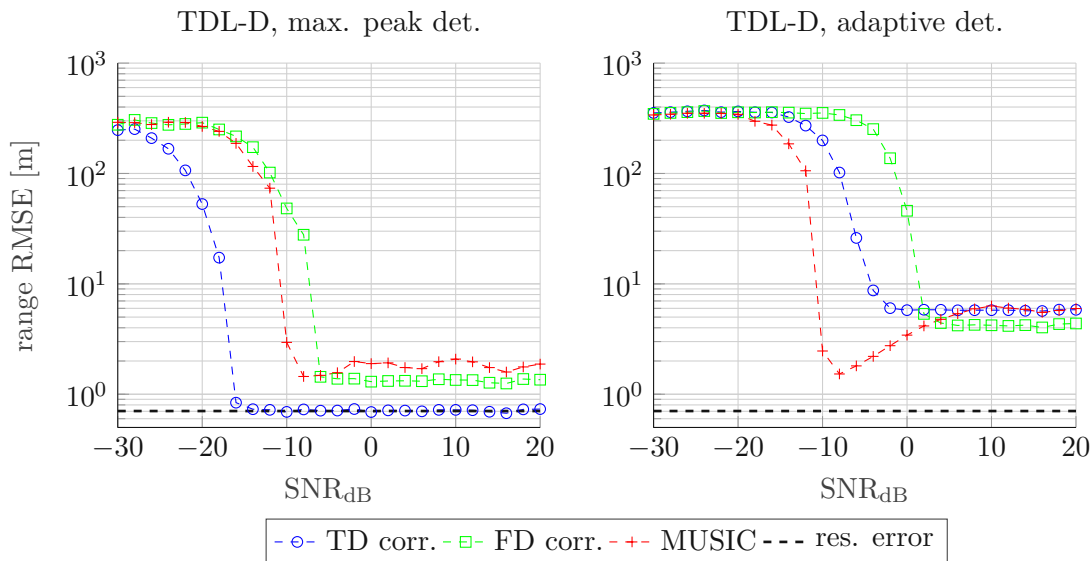
Figure 3.17: Ranging performance comparison for different delay profiles in LOS channels, $B = 100$ MHz, $DS = 129$ ns

starts to drop for lower SNR as compared to the other delay profiles, with the frequency domain correlation method being most sensitive to noise. We explain this behavior with the ability of the MUSIC algorithm to separate multipath components even in lower SNR ranges. In two out of three channel models, MUSIC yields the lowest ranging error, however with only a small performance gap to the other methods. Furthermore, it becomes again visible that the chosen threshold highly affects the performance of the adaptive threshold detector also in NLOS channels, since the ranging error might even rise again in low SNR regimes if the first multipath component is the strongest.

The simulation results for the LOS channels are visualized in figure 3.17. We observe a similar trend of the ranging error as compared to the results for the AWGN channel, with the combination of time domain correlation delay profile and maximum peak detector yielding the highest accuracy. Again, the adaptive threshold detector performs worse since it missdetects correlation side lobes as the main delay peak.

The curves in figure 3.18 visualize the effect of a varying transmission bandwidth B on the ranging accuracy. Note that increasing the bandwidth also increases the received noise power, hence when the bandwidth is doubled, the curves in figure 3.18 are moved to the right by 3 dB. Furthermore, we only show results for the time domain correlation delay profile, since the behavior is similar for the other delay profiles considered in the thesis. The simulations confirm that an increased bandwidth improves the ranging accuracy for the bandwith values investigated in our experiments, due to higher time delay resolution. This is true for the adaptive threshold detector in both LOS (TDL-C) and NLOS (TDL-D) channels (behavior similar for channels not depicted in plots), while the maximum peak detector only profits from increased bandwith in the LOS case. In
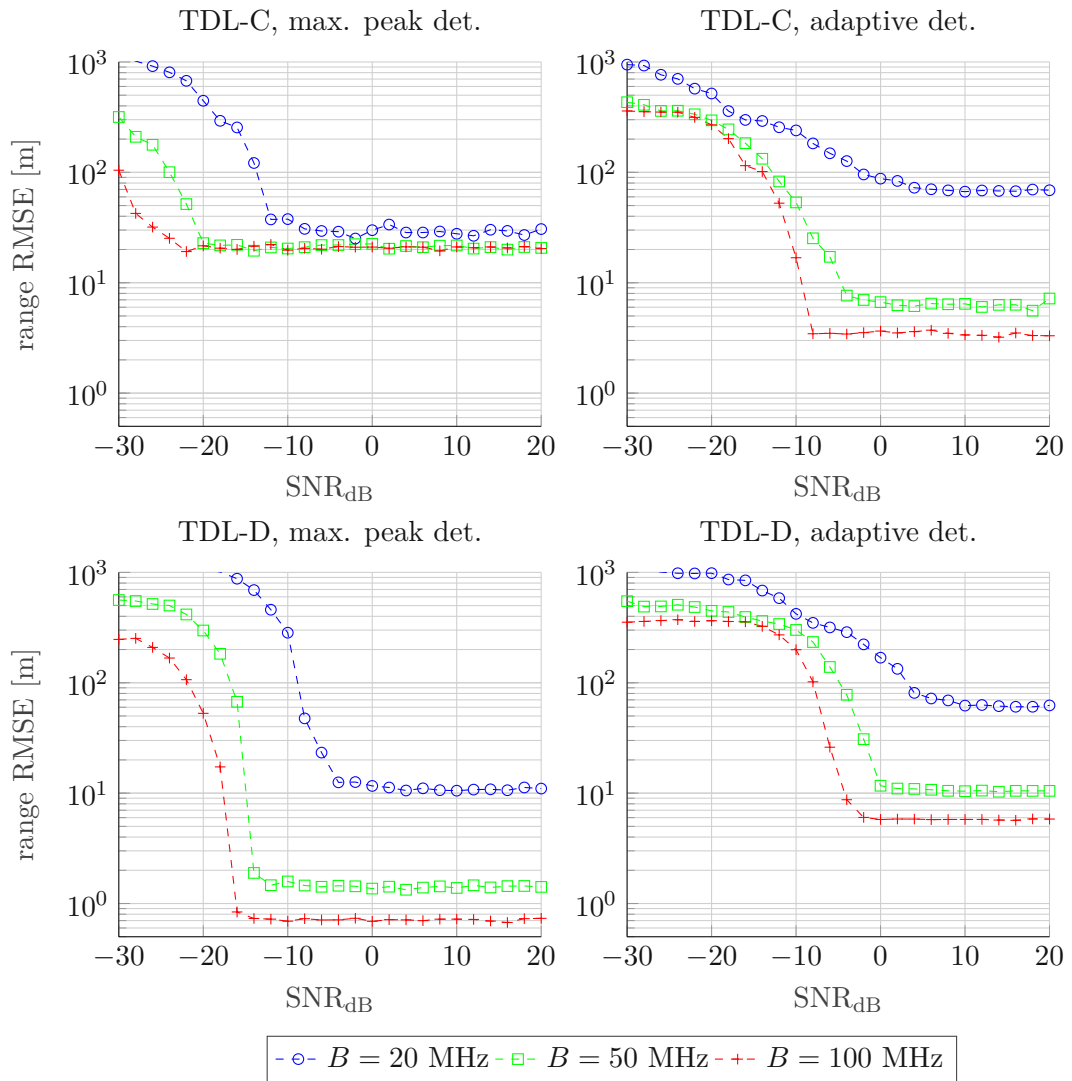
Figure 3.18: Ranging performance comparison with varying transmission bandwidth B (delay profile: time domain correlation), $DS = 129$ ns
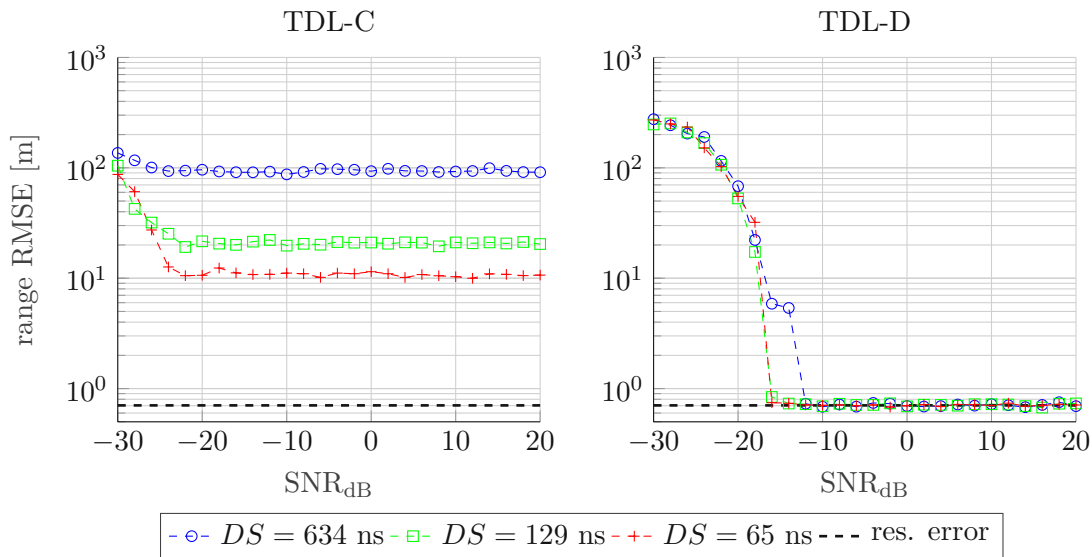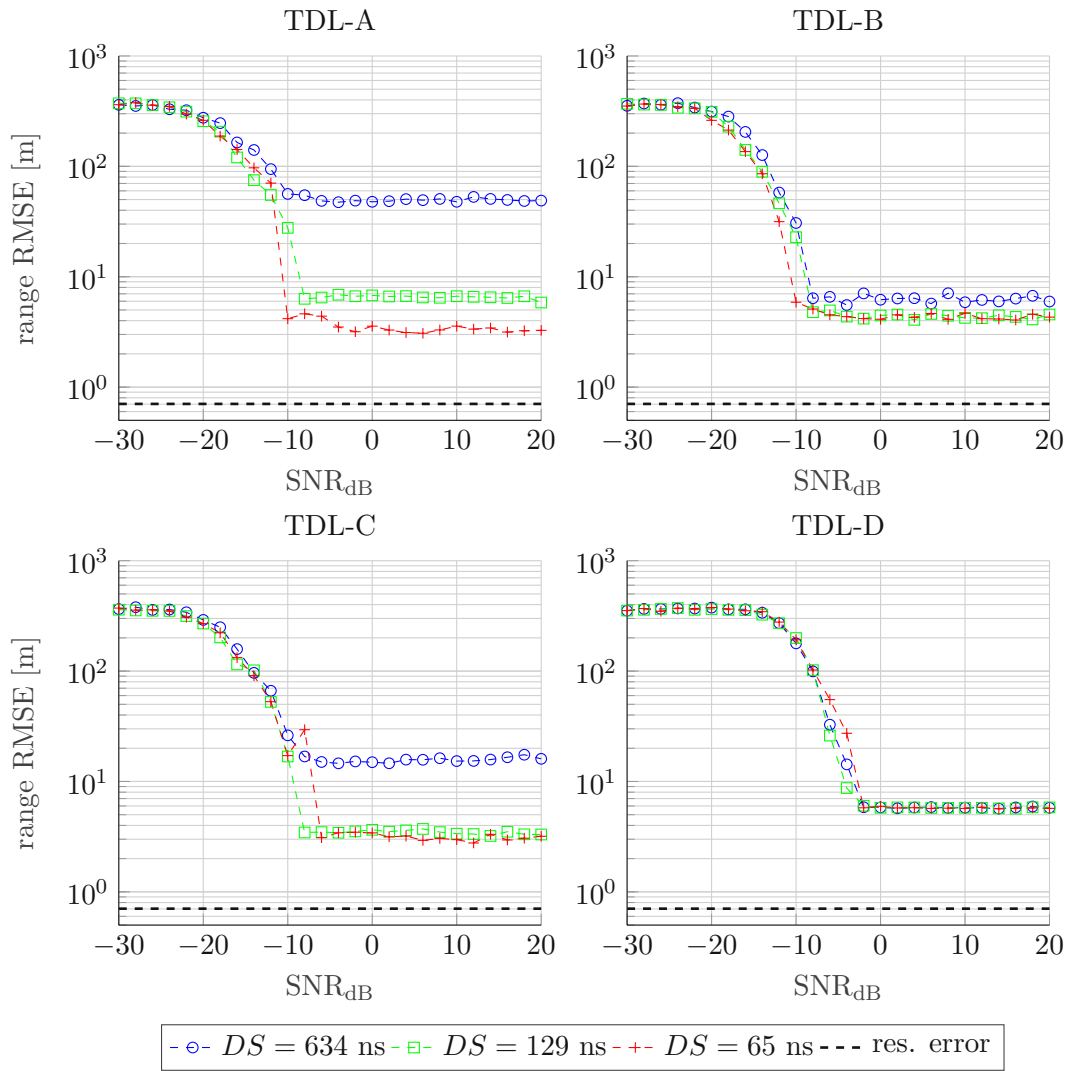
38

Figure 3.19: Ranging performance comparison with varying delay spread DS (delay profile: time domain correlation, delay peak detector: maximum peak), $B = 100$ MHz

NLOS situations, the maximum peak detector of course fails to identify the direct path, hence the ranging error approximately saturates at the same value for all the simulated bandwidth values.

Finally, we simulate the effect of channel delay spread DS on the ranging accuracy. Note that we only show results for the time domain correlation delay profile, since the behavior is similar for the other delay profiles considered in the thesis. Figure 3.19 shows how the ranging error yielded by the maximum peak detector is affected by varying the delay spread. In the NLOS (TDL-C) channel, ranging accuracy decreases with increasing delay spread. This is because in channels with a long delay spread the delay peak resulting from the shortest path might be farther away from the detected strongest peak - as opposed to channels with short delay spread. That behavior also explains why varying the delay spread in the value range simulated in this thesis does not have a significant effect on the ranging performance of the maximum peak detector in the LOS (TDL-D) channel. Figure 3.20 shows the delay spread variation simulation results for the adaptive threshold detector. We can observe that also for the adaptive threshold detector, a shorter delay spread can have a favorable effect on ranging accuracy in some NLOS channels (TDL-A/C). This is due to the fact that if the weak first peak cannot be detected, the time delay estimation error will be lower due to the shorter interval between peaks as compared to longer delay spread values. In other NLOS channels (TDL-B), where the delay peak resulting from the shortest is close to the strongest peak, or in LOS channels (TDL-D), delay spread variation in the value range simulated in this thesis does not have a significant effect on the ranging accuracy.

Figure 3.20: Ranging performance comparison with varying delay spread DS (delay profile: time domain correlation, delay peak detector: adaptive threshold), $DS = 129$ ns

CHAPTER 4

Position estimation with TDOA information

In chapter 2, an overview over various approaches suitable for positioning in cellular networks was given. Chapter 3 presented the challenges imposed by time delay estimation in urban vehicular scenarios and introduced methods for tackeling the problem. In the following chapter, we investigate how downlink propagation time information can be used to estimate the position of a vehicle, also referred to as multilateration. More concretely, we focus on TDOA positioning, which only requires timing synchronization between the BSs, as opposed to TOA positioning, which additionally requires timing synchronization between all BSs and the UE at the vehicle [ZB11]. This is desirable, since synchronization between BSs is also required by other features of the cellular network and thus already specified for 5G-NR by the 3GPP standard [rGPPG20a]. Furthermore, note that TDOA is supported by the standard, while TOA-based positioning is not [rGPPG22]. The key components of such a positioning system based on time delay measurements obtained from multiple received reference signals $\boldsymbol{y}_i$, $i = 0, \ldots, N_{BS} - 1$ are visualized in figure 4.1.

The chapter is structured as follows: Section 4.1 introduces the system model for the hyperbolic positioning problem with TDOA information and section 4.2 presents solution methods to the hyperbolic problem in order to estimate the UE position. Finally, section 4.3 introduces the simulation setup and standard-compliant path loss models for
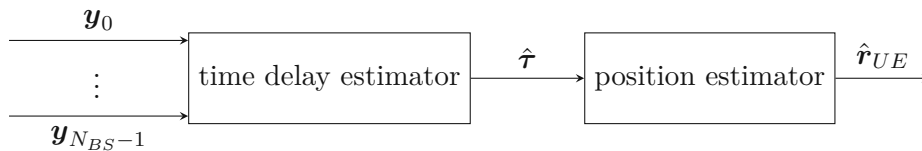
Figure 4.1: Positioning procedure based on time delay estimates in a cellular network

evaluating the performance of the positioning methods and summarizes the simulation results.

4.1 System model

To begin with, consider a cellular network composed of N_{BS} transmitting BSs, with their known 3D position coordinates

$$\boldsymbol{r}_{BS,i} = [x_{BS,i}, y_{BS,i}, z_{BS,i}]^T, \ i = 0, \ldots, N_{BS} - 1 \tag{4.1}$$

and a receiving UE with the unknown 3D position $\boldsymbol{r}_{UE} = [x_{UE}, y_{UE}, z_{UE}]^T$. Note that all following derivations are also valid for the 2D positioning case - for that purpose the z coordinate has to be omitted. The ranges between BSs and UE are given by

$$\boldsymbol{d} = [d_0, \ldots, d_{N_{BS}-1}]^T \in \mathbb{R}_{\geq 0}^{N_{BS} \times 1}, \text{ with } d_i = ||\boldsymbol{r}_{BS,i} - \boldsymbol{r}_{UE}||_2 \tag{4.2}$$

$$= \sqrt{||\boldsymbol{r}_{BS,i}||_2^2 - 2\boldsymbol{r}_{BS,i}^T \boldsymbol{r}_{UE} + ||\boldsymbol{r}_{UE}||_2^2} \tag{4.3}$$

$$= \sqrt{(x_{BS,i} - x_{UE})^2 + (y_{BS,i} - y_{UE})^2 + (z_{BS,i} - z_{UE})^2}. \tag{4.4}$$

Furthermore, as a result of employing methods from chapter 3, unsynchronized estimates of the propagation time delay between the UE and every BS are assumed to be available:

$$\hat{\boldsymbol{\tau}} = [\hat{\tau}_0, \ldots, \hat{\tau}_{N_{BS}-1}]^T \in \mathbb{R}_{\geq 0}^{N_{BS} \times 1}. \tag{4.5}$$

The true delay values $\boldsymbol{\tau}$ are related to the ranges by $c_0 \boldsymbol{\tau} = \boldsymbol{d}$, where c_0 is the propagation speed. The i-th delay estimate can be modelled as $\hat{\tau}_i = \tau_i + \epsilon_i + b_{clock}$, where ϵ_i is the estimation error and b_{clock} is a clock bias due to the non-present time synchronization between BSs and UE. Furthermore, the estimation error might include a significant bias resulting from NLOS propagation. Taking the difference of two delay estimates from different BSs

$$\hat{\tau}_i - \hat{\tau}_j = \tau_i + \epsilon_i + b_{clock} - \tau_j - \epsilon_j - b_{clock} = (\tau_i + \epsilon_i) - (\tau_j + \epsilon_j), \ i \neq j \tag{4.6}$$

eliminates the clock bias. Hence, by designating one BS as a reference point, the need for timing synchronization between BSs and UE vanishes. Without loss of generality, it is assumed that $\boldsymbol{r}_0^{BS}$ is the position of the reference BS. In a next step, the $N_{BS} - 1$ TDOA values are computed from the time delay estimates
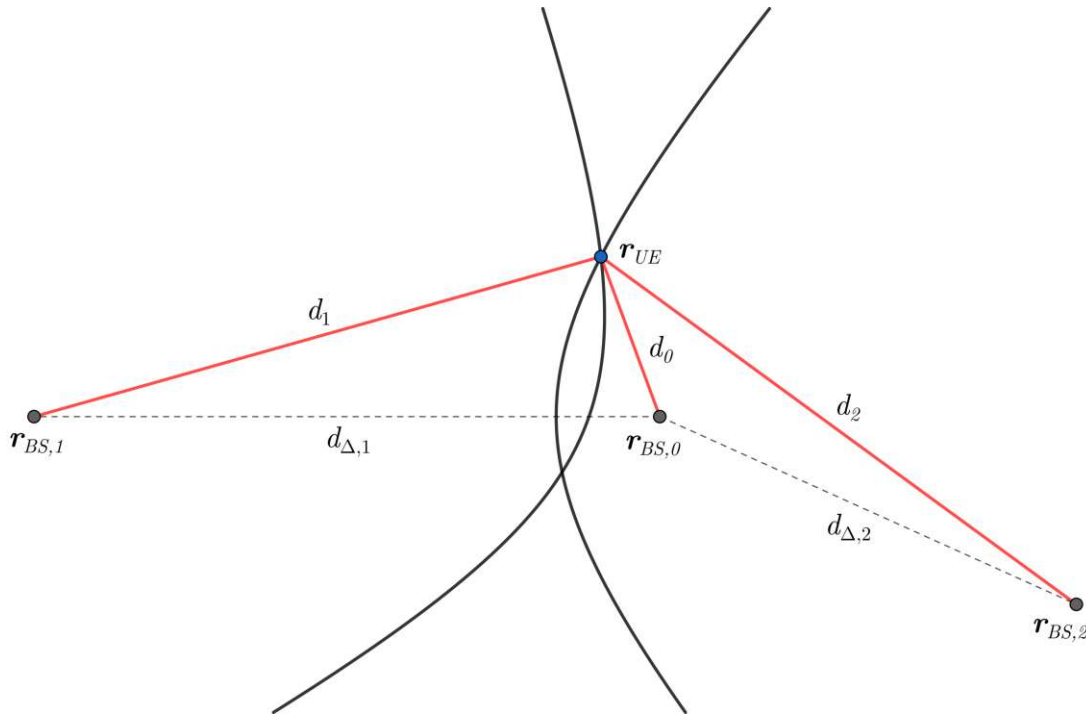
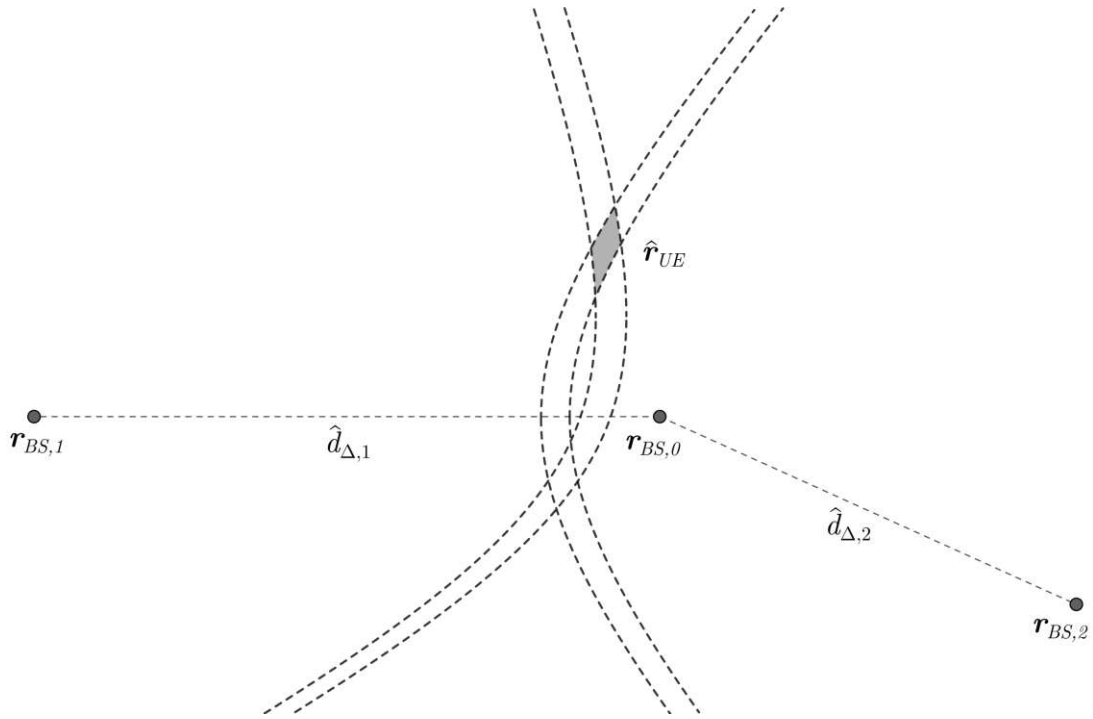Figure 4.2: Hyperbolic positioning with perfect range information, $N_{BS} = 3$

$$\hat{\boldsymbol{\tau}}_\Delta = [\hat{\tau}_1 - \hat{\tau}_0, \ldots, \hat{\tau}_{N_{BS}-1} - \hat{\tau}_0]^T \in \mathbb{R}_{\geq 0}^{(N_{BS}-1)\times 1}, \tag{4.7}$$

with their corresponding range differences

$$\boldsymbol{d}_\Delta = [d_1 - d_0, \ldots, d_{N_{BS}-1} - d_0]^T \in \mathbb{R}^{(N_{BS}-1)\times 1}. \tag{4.8}$$

One major tradeoff of the TDOA positioning method becomes visible immediately: the delay measurement of the reference BS must be sacrificed for synchronization purposes and is thus not available to the subsequent positioning algorithm. As a consequence, the TDOA positioning method requires $N_{BS} \geq dim+1$, where dim refers to the dimensionality of the coordinate system. The TOA positioning method on the other hand only requires $N_{BS} \geq dim$. Combining the TDOA values and range differences, a set of $N_{BS} - 1$ non-linear equations is introduced:

$$\hat{\boldsymbol{d}}_\Delta = \boldsymbol{d}_\Delta, \text{ where } \hat{\boldsymbol{d}}_\Delta = c_0\hat{\boldsymbol{\tau}}_\Delta. \tag{4.9}$$

43

Figure 4.3: Hyperbolic positioning with range uncertainty, $N_{BS} = 3$

From a geometric point of view, each of the equations in 4.9 describes a hyperbola, hence the TDOA positioning method is often referred to as hyperbolic positioning. The position of the UE is located at the intersection of these hyperbolas, as shown in figure 4.2. In practice, the equations in 4.9 only hold approximately and the hyperbolas do not exactly intersect in a single point due to the erroneous estimates $\hat{\boldsymbol{\tau}}_\Delta$ of $\boldsymbol{\tau}_\Delta$, as depicted in figure 4.3. This leads to an approximate estimate $\hat{\boldsymbol{r}}_{UE}$ of the unknown UE position $\boldsymbol{r}_{UE}$. Additional estimation errors are introduced due to linearization or non-linear optimization of the equations in 4.9. In the following section, methods for obtaining a solution for the hyperbolic equations are presented.

4.2 Hyperbolic positioning methods

4.2.1 Friedlander's method

In this section we present the hyperbolic positioning method discovered by Friedlander [Fri87]. First, we rearrange and square the equations 4.9 to form $d_i^2 = (\hat{d}_{\Delta,i} + d_0)^2$, $i = 1, \ldots, N_{BS} - 1$. The squared ranges from equation 4.2 can now be written as

$$\hat{d}_{\Delta,i}^2 + 2\hat{d}_{\Delta,i}d_0 + d_0^2 = ||\boldsymbol{r}_{BS,i}||_2^2 - 2\boldsymbol{r}_{BS,i}^T \boldsymbol{r}_{UE} + ||\boldsymbol{r}_{UE}||_2^2 \tag{4.10}$$

and if the squared range of the reference BS d_0^2, obtained by setting $i = 0$ in 4.2, is substracted from the result above, we end up with

$$\hat{d}_{\Delta,i}^2 + 2\hat{d}_{\Delta,i}d_0 = ||\boldsymbol{r}_{BS,i}||_2^2 - 2(\boldsymbol{r}_{BS,i} - \boldsymbol{r}_{BS,0})^T\boldsymbol{r}_{UE} - ||\boldsymbol{r}_{BS,0}||_2^2. \qquad (4.11)$$

Writing this result in matrix-vector notation

$$\boldsymbol{S}\boldsymbol{r}_{UE} = \boldsymbol{u} - d_0\hat{\boldsymbol{d}}_\Delta \qquad (4.12)$$

with

$$\boldsymbol{S} = \begin{bmatrix} \boldsymbol{r}_{BS,1}^T - \boldsymbol{r}_{BS,0}^T \\ \vdots \\ \boldsymbol{r}_{BS,N_{BS}-1}^T - \boldsymbol{r}_{BS,0}^T \end{bmatrix} \in \mathbb{R}^{(N_{BS}-1)\times dim} \qquad (4.13)$$

and

$$\boldsymbol{u} = \frac{1}{2}\begin{bmatrix} ||\boldsymbol{r}_{BS,1}||_2^2 - ||\boldsymbol{r}_{BS,0}||_2^2 - \hat{d}_{\Delta,1}^2 \\ \vdots \\ ||\boldsymbol{r}_{BS,N_{BS}-1}||_2^2 - ||\boldsymbol{r}_{BS,0}||_2^2 - \hat{d}_{\Delta,N_{BS}-1}^2 \end{bmatrix} \in \mathbb{R}^{(N_{BS}-1)\times 1}, \qquad (4.14)$$

immediately shows that this form is now linear in the unknown $\boldsymbol{r}_{UE}$, with the unknown nuisance parameter d_0 present. The trick in [Fri87] is to remove this nuisance parameter by premultiplying the matrix-vector equation with a matrix $\boldsymbol{M} = (\boldsymbol{I}_{(N_{BS}-1)\times(N_{BS}-1)} - \boldsymbol{Z})\boldsymbol{D}^{-1}$, which is constructed such that $\boldsymbol{M}\hat{\boldsymbol{d}}_\Delta = \boldsymbol{0}_{(N_{BS}-1)\times 1}$, hence $\hat{\boldsymbol{d}}_\Delta$ is in its null-space of $\boldsymbol{M}$. The matrix $\boldsymbol{M}$ is constructed with $\boldsymbol{D} = \text{diag}\{\hat{\boldsymbol{d}}_\Delta\}$ and the circular shift matrix

$$\boldsymbol{Z} = \begin{bmatrix} 0 & 1 & 0 & \dots & 0 \\ 0 & 0 & 1 & \dots & 0 \\ & \ddots & \ddots & \ddots & \\ 0 & 0 & 0 & \dots & 1 \\ 1 & 0 & 0 & \dots & 0 \end{bmatrix} \in \mathbb{R}^{(N_{BS}-1)\times(N_{BS}-1)} \qquad (4.15)$$

Multiplying equation 4.2.1 by $\boldsymbol{M}$ yields

45

$$MSr_{UE} = Mu. \tag{4.16}$$

This equation can now be solved by forming the Moore-Penrose pseudoinverse of MS and the estimated UE position is obtained as the linear least squares (LS) solution of equation 4.16 given by

$$\hat{r}_{UE} = (S^T M^T M S)^{-1} S^T M^T M u. \tag{4.17}$$

Note that $N_{BS} > dim + 1$ is required in order for MS to be non-singular.

Advandtages of this method include that it can potentially use an unlimited number of TDOA measurements, that it does not require a-priori information and that it is relatively simple to implement and compute. The major disadvantage and source of error is that the noisy time delay measurements are not weighted according to their estimation confidence and hence are treated as equally accurate, altough the method can be extended to incorporate this information. Another drawback of the method is that it simply eliminates the nuisance parameter d_0 rather than estimating it as well.

4.2.2   Chan's method

In this section, the solution method proposed by Chan et al. [CH94a, CH94b] is investigated. Without loss of generality, for the following derivations it is assumed that the reference BS with coordinates r_0^{BS} is placed at the origin, which can be achieved in a straight-forward manner by shifting the reference coordinate system. Setting $r_0^{BS} = \mathbf{0}$ simplifies equation 4.10 to

$$\hat{d}_{\Delta,i}^2 + 2\hat{d}_{\Delta,i}d_0 = ||r_{BS,i}||_2^2 - 2r_{BS,i}^T r_{UE}. \tag{4.18}$$

The method aims to solve this problem in a two-step procedure. First, assume r_{UE} and the nuisance parameter d_0 to be independent and combine them to the parameter vector $u_1 = [r_{UE}^T, d_0]^T \in \mathbb{R}^{(dim+1)\times 1}$. Rearranging equation 4.18 and writing it in matrix-vector notation yields

$$h_1 = G_1 u_1 \tag{4.19}$$

with

$$\boldsymbol{h}_1 = \begin{bmatrix} \hat{d}_{\Delta,1}^2 - ||\boldsymbol{r}_{BS,1}||_2^2 \\ \vdots \\ \hat{d}_{\Delta,N_{BS}-1}^2 - ||\boldsymbol{r}_{BS,N_{BS}-1}||_2^2 \end{bmatrix} \in \mathbb{R}^{(N_{BS}-1)\times 1} \qquad (4.20)$$

and

$$\boldsymbol{G}_1 = -2 \begin{bmatrix} \boldsymbol{r}_{BS,1}^T & \hat{d}_{\Delta,1} \\ \vdots & \vdots \\ \boldsymbol{r}_{BS,N_{BS}-1}^T & \hat{d}_{\Delta,N_{BS}-1} \end{bmatrix} \in \mathbb{R}^{(N_{BS}-1)\times(dim+1)}. \qquad (4.21)$$

The ML estimator of $\boldsymbol{u}_1$ is given by weighted LS solution of equation 4.26

$$\hat{\boldsymbol{u}}_1 = (\boldsymbol{G}_1^T \boldsymbol{W}_1 \boldsymbol{G}_1)^{-1} \boldsymbol{G}_1^T \boldsymbol{W}_1 \boldsymbol{h}_1 \qquad (4.22)$$

with the weighting matrix

$$\boldsymbol{W}_1 = \frac{1}{4c_0^2} \boldsymbol{B}_1^{-1} \boldsymbol{C}_{\boldsymbol{\tau}_{\boldsymbol{\Delta}}}^{-1} \boldsymbol{B}_1^{-1}, \; \boldsymbol{B}_1 = \mathrm{diag}\{[d_1, \ldots, d_{N_{BS}-1}]^T\}. \qquad (4.23)$$

The matrix $\boldsymbol{C}_{\boldsymbol{\tau}_{\boldsymbol{\Delta}}} \in \mathbb{R}^{(N_{BS}-1)\times(N_{BS}-1)}$ expresses the reliability of the measurements contained in $\hat{\boldsymbol{\tau}}_\Delta$. Following an idea from [Men13], this covariance matrix is constructed as

$$\boldsymbol{C}_{\boldsymbol{\tau}_{\boldsymbol{\Delta}}} = \boldsymbol{D}\mathrm{diag}\{[\sigma_{\tau,0}^2, \ldots, \sigma_{\tau,N_{BS}-1}^2]^T\}\boldsymbol{D}^T, \qquad (4.24)$$

with $\boldsymbol{D} = [-\boldsymbol{1}_{(N_{BS}-1)\times 1}, \boldsymbol{I}_{(N_{BS}-1)\times(N_{BS}-1)}] \in \mathbb{R}^{(N_{BS}-1)\times(N_{BS})}$ and where $\sigma_{\tau,i}^2, i = 0, \ldots, N_{BS} - 1$ are the variances of the unsynchronized time delay estimates for all BS-UE links in the network. In this thesis, we approximate these values by the receiver SNR of the links, i.e. $\sigma_{\tau,i}^2 \approx 1/SNR_i, i = 0, \ldots, N_{BS} - 1$. This is justified because the simulation results from the previous chapter showed that a high SNR is necessary in order to obtain accurate time delay measurements. Note that the values from $\boldsymbol{d}$ used to construct $\boldsymbol{B}_1$ are of course unknown, hence it is necessary to first approximate the estimated parameter vector $\hat{\boldsymbol{u}}_1$ by

$$\hat{\boldsymbol{u}}_1 \approx (\boldsymbol{G}_1^T \boldsymbol{C}_{\boldsymbol{\tau}_{\boldsymbol{\Delta}}}^{-1} \boldsymbol{G}_1)^{-1} \boldsymbol{G}_1^T \boldsymbol{C}_{\boldsymbol{\tau}_{\boldsymbol{\Delta}}}^{-1} \boldsymbol{h}_1. \qquad (4.25)$$

This result can be used to approximate $\boldsymbol{B}_1$ in order to compute equation 4.22. Note that the result is now only an approximation of the ML estimator. Repeated computation of equation 4.22 with refined approximations of $\hat{\boldsymbol{u}}_1$ can improve the overall estimation accuracy. In a second step, it is necessary to account for the actual dependence between $\boldsymbol{r}_{UE}$ and d_0 and hence to eliminate d_0 from the result. A second equation set

$$\boldsymbol{h}_2 = \boldsymbol{G}_2 \boldsymbol{u}_2. \tag{4.26}$$

is obtained by squaring the elements of $\hat{\boldsymbol{u}}_1$, with $\boldsymbol{h}_2 = [\hat{u}_{1,0}^2, \ldots, \hat{u}_{1,dim-1}^2]^T$, $\boldsymbol{u}_2 = [r_{UE,0}^2, \ldots, r_{UE,dim-1}^2]$ and

$$\boldsymbol{G}_2 = \begin{bmatrix} \boldsymbol{I}_{dim \times dim} \\ \boldsymbol{1}_{dim \times 1}^T \end{bmatrix} \in \mathbb{R}^{(dim+1) \times dim}. \tag{4.27}$$

The solution to this equation is obtained by the second approximated ML estimator

$$\hat{\boldsymbol{u}}_2 \approx (\boldsymbol{G}_2^T \boldsymbol{W}_2 \boldsymbol{G}_2)^{-1} \boldsymbol{G}_2^T \boldsymbol{W}_2 \boldsymbol{h}_2. \tag{4.28}$$

The second weighting matrix is given by

$$\boldsymbol{W}_2 = \frac{1}{4} \boldsymbol{B}_2^{-1} \boldsymbol{G}_1^T \boldsymbol{W}_1 \boldsymbol{G}_1 \boldsymbol{B}_2^{-1}, \quad \boldsymbol{B}_1 = \text{diag}\{[u_{1,0}, \ldots, u_{1,dim-1}]\}. \tag{4.29}$$

To obtain the desired estimate of the UE position, we compute

$$\hat{\boldsymbol{r}}_{UE} = \text{diag}\{[sgn(\hat{u}_{2,0}), \ldots, sgn(\hat{u}_{2,dim-1})]\}\sqrt{\hat{\boldsymbol{u}}_2}, \tag{4.30}$$

where the signs of the elements in $\hat{\boldsymbol{u}}_2$ are preserved to resolve the ambiguity due to the square root. Note that the $\hat{\boldsymbol{r}}_{UE}$ has to be transformed back to the original coordinate system if the reference BS was moved to the origin in the beginnig of the algorithm.

Advantages of the method include that it is an approximation of the ML estimator, the weighting of the TDOA measurements according to their reliability and the fact that the nuisance parameter d_0 is estimated as well rather than simply being eliminated. Furthermore, this method is able to potentially process an unlimited number of TDOA estimates. Disadvantages are the more involved computation due to the multi-step weighted LS procedure and the required a-priori information.

4.3 Simulations

4.3.1 Path loss model

In order to evaluate the positioning methods, it is necessary to incorporate the effect of the physical distance between BS and UE on the radio signal propagation into the simluation setup. This is done by employing a so-called path loss model. The most basic path loss model is known as the Friis equation or free space model [PP00] and describes the ratio PL_{fs} between the received signal power P_{rx} and the transmit power P_{tx} in an area free of obstruction:

$$PL_{fs} = \frac{P_{rx}}{P_{tx}} = G_{tx} G_{rx} \left(\frac{c_0}{4\pi f_c d} \right)^2. \tag{4.31}$$

The values G_{tx} and G_{rx} refer to the transmitter and receiver gain respectively, while f_c denotes the carrier frequency of the modulated pass-band signal, d denotes the distance between transmitter and receiver and c_0 is the propagation speed. This equation reveals a fundamental property of radio wave propagation, which states that the received power decreases with the square of the distance. The free space model can also be written in the convenient logarithmic form

$$PL_{fs|dB} = P_{tx|dBm} - P_{rx|dB} = G_{tx|dB} + G_{rx|dB} + 20 \log_{10} \left(\frac{c_0}{4\pi f_c d} \right) \tag{4.32}$$

in order to compute the path loss in decibels.

For the simulations in this thesis, we use more sophisticated path loss models specified by the UMi and Urban Macrocell (UMa) scenarios from the 3GPP standard [rGPPG18]. These models are taylored to propagation conditions in urban settings and are able to generate a different path loss for LOS and NLOS links.

4.3.2 Setup

The simulation setup used in this section builds on top of the simulation framework from chapter 3. In order to perform positioning, we introduce a cellular network geometry in the form of BS and UE positions, which can be used in conjunction with a path loss model as described above. The layout of the BSs in the setup is given by a hexagonal grid, which is common for simulating cellular networks and used by many authors, e.g. in [dPRLSSG+12, DZW+20]. The AWGN is now modelled as thermal noise at the receiver [MATb], with average noise power

$$\sigma_n^2 = k_B * T_s * (T_{rx} + 290 \cdot (10^{\frac{NF}{10}} - 1)). \tag{4.33}$$
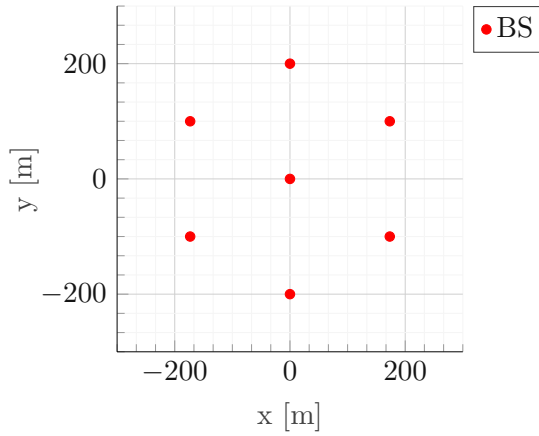
Figure 4.4: UMi scenario network layout

Figure 4.5: UMa scenario network layout

Name	Value
Pathloss model	3GPP UMi
Delay spread	$DS = 129$ ns
Number of BSs	$N_{BS} = 7$
Transmit power	$P_{tx} = 24$ dBm
Inter-station distance	200 m
BS height	$z_{BS} = 10$ m
UE height	$z_{UE} = 1.5$ m

Table 4.1: UMi scenario parameters

Name	Value
Pathloss model	3GPP UMa
Delay spread	$DS = 363$ ns
Number of BSs	$N_{BS} = 7$
Transmit power	$P_{tx} = 24$ dBm
Inter-station distance	500 m
BS height	$z_{BS} = 25$ m
UE height	$z_{UE} = 1.5$ m

Table 4.2: UMa scenario parameters

The value k_B refers to the Boltzmann constant[1], T_s is the sampling rate of the OFDM transmission system, T_{rx} refers to the receiver temperature and NF represents the receiver noise figure. The reference signal is transmitted with a certain transmit power P_{tx}. The received signal is now given by

$$\boldsymbol{y} = \frac{1}{\sqrt{PL}}(\boldsymbol{h} * \boldsymbol{x}) + \boldsymbol{n}, \tag{4.34}$$

where PL refers to the pathloss value obtained from the selected path loss model. Note that in this setup all BSs transmit only reference signals. Furthermore, inter-cell interference free transmission is assumed, which can be achieved by an appropriate PRS configuration as described in section 3.1.2. In a real system we would of course expect some form of interference, e.g. due to the simultaneous transmission of data and PRS on interfering BSs. Investigating the effect of such interference on the positioning accuracy is however not in the scope of this thesis. For LOS and NLOS links a respective TDL

---

[1]$k_B = 1.380649 \cdot 10^{-23} \; \frac{\text{J}}{\text{K}}$

Name	Value
Monte Carlo repetitions	$N_{mc} = 1000$
Transmit bandwidth	$B = 100$ MHz
Number of subcarriers	$N_{sc} = 3276$
FFT size	$N_{FFT} = 4096$
Sampling rate	$T_s = 128$ MHz
Cyclic prefix length	$N_{cp} = 288$
Subcarrier spacing	$\Delta f_{sc} = 30$ kHz
Numerology	$\mu = 1$
PRS symbols per slot	$L_{PRS} = 12$
PRS comb size	$K_{comb}^{PRS} = 2$
LOS channel model	TDL-D
NLOS channel model	TDL-C
Carrier frequency	3 GHz
Transmit power	$P_{tx} = 24$ dBm
Receiver noise figure	$NF = 9$ dB
Receiver temperature	$T_{rx} = 290$ K

Table 4.3: Common simulation parameters

channel model is selected from the standard [rGPPG18] and applied as explained in section 3.5.1. As for the propagation delay estimation method for this simulation setup, we employ the delay profile computation based on time domain correlation in combination with the adaptive threshold detector, as introduced in sections 3.3.1 and 3.4.2. In order to asses the quality of the positioning methods in scenarios with many NLOS links, we conduct simulations for a steadily increasing number of NLOS links, starting of with only LOS links and ending with a situation where the UE is in NLOS for all BSs. This results in N_{BS} different simulation configurations, where the distribution of the Euclidean position error

$$E_{pos} = ||\boldsymbol{r}_{UE} - \hat{\boldsymbol{r}}_{UE}||_2 \tag{4.35}$$

in each configuration is approximated by sampling from random UE positions uniformly distributed over the region of interest in N_{mc} Monte Carlo repetitions. We consider two different simulation scenarios, which are the already introduced UMi and UMa scenarios specified by the standard [rGPPG18]. Their respective network layouts are shown in figures 4.4 and 4.5 and their distinct simulation parameters are listed in tables 4.1 and 4.2. Table 4.3 summarizes all common parameters relevant for the setup in this chapter.
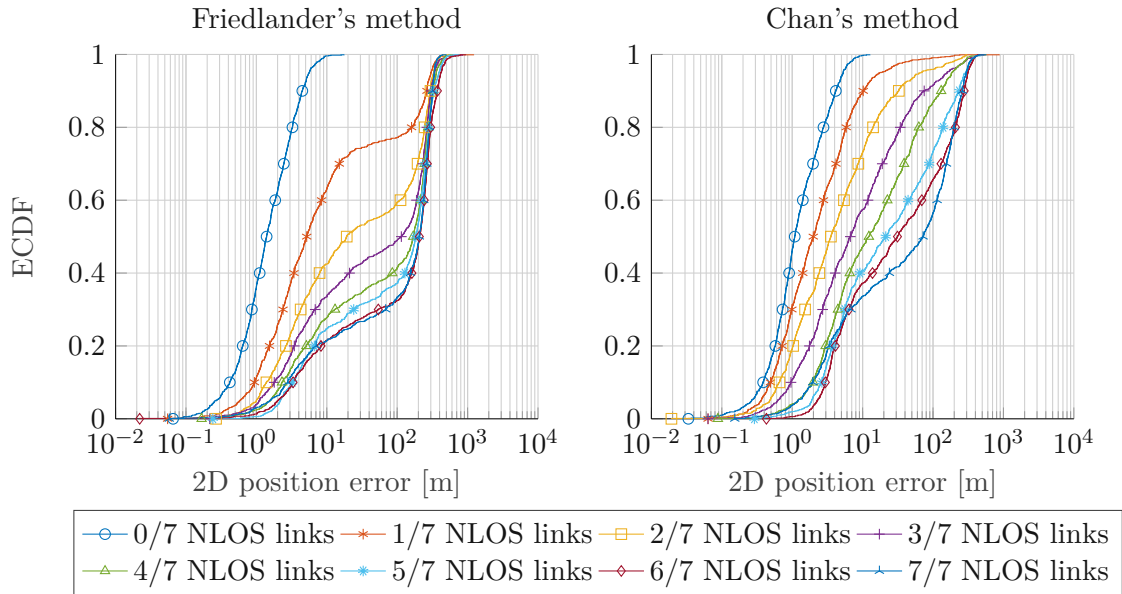
Figure 4.6: UMi scenario, $dim = 2$

4.3.3 Results

Looking at the simulation results for the two-dimensional positioning problem in the UMi scenario in figure 4.6, reveals the significant performance difference between Friedlander's and Chan's method. While the positioning accuracy of both methods is similar in case all links are in LOS (i.e. 0/7 NLOS links), Chan's method is clearly superior in situations where links switch from LOS to NLOS. This confirms that weighting the TDOA measurements in accordance with their reliability and estimating nuisance parameters rather than discarding them can bring a performance improvement. Note however, that Chan's method still suffers under NLOS propagation and the performance also degrades if most links are in NLOS. Figure 4.7 indicates that mostly UE positions outside the fundamental hexagon are affected by this performance degradation, the reason being that the increased path loss due to higher distances decreases the probability that the direct path in NLOS will be detected in the noise. The simulation results for the UMa scenario show a similar, even more articulate performance difference between Friedlander's and Chan's method for NLOS TDOA positioning, as can be seen in figure 4.8. Compared to the UMa scenario, the positioning accuracy of both methods in the UMa scenario degrades stronger in case of multiple NLOS links, which is, as elaborated before, due to increased distances in the scenario.

The simulation results for the three-dimensional positioning problem reveal a similar distribution, but overall strongly degraded positioning accuracy as compared to the two-dimensional case. This can verified in figure 4.9 for the UMi scenario and in figure 4.10 for the UMa scenario. The reason for this accuracy gap between $dim = 2$ and $dim = 3$ is mainly due to the reduced redundancy in the $dim = 3$. For three-dimensional
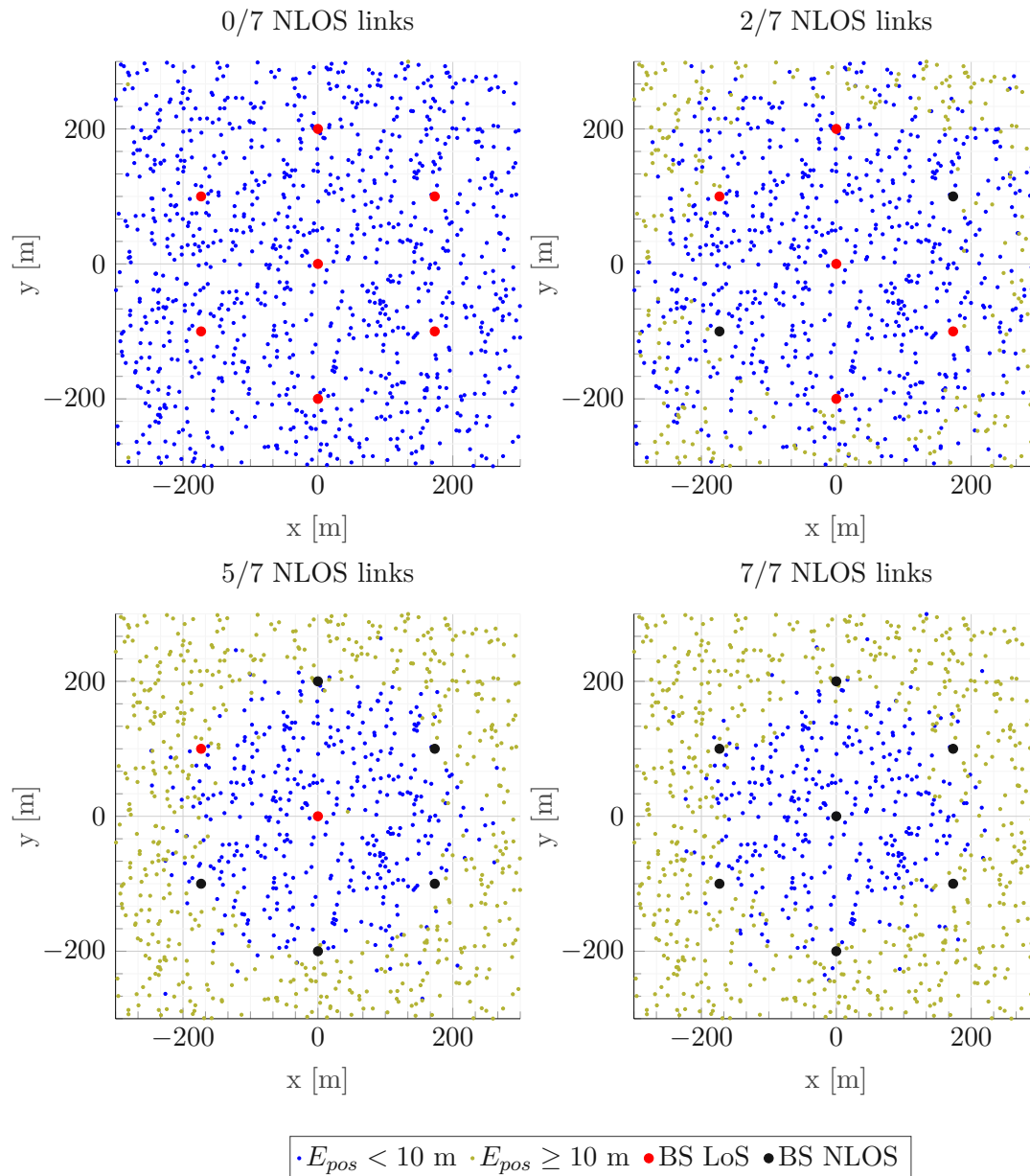
Figure 4.7: UMi scenario, spatial distribution of the 2D position error, $dim = 2$

Friedlander's method

Chan's method
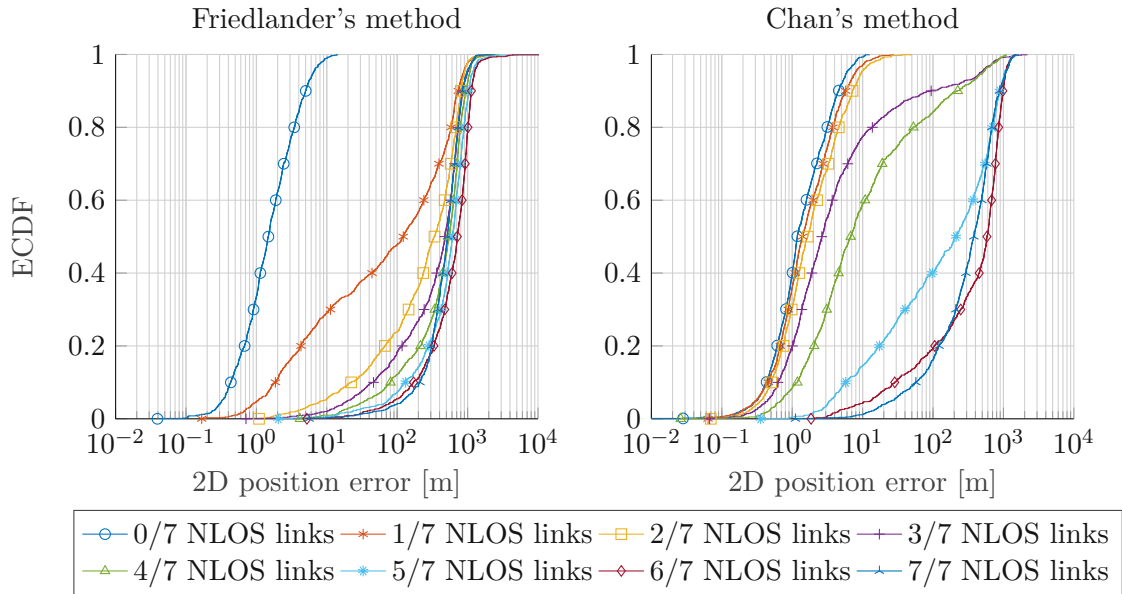
Figure 4.8: UMa scenario, $dim = 2$

hyperbolic positioning, already $N_{BS} = 5$ BSs are required just to obtain a unique solution, as compared to $N_{BS} = 4$ in the two-dimensional problem. Hence, in this hexagonal grid scenario with a total of 7 BSs, less redundant range measurements remain in order to make up for unreliable values - confirming that three-dimensional TDOA positioning is less accurate than two-dimensional positioning for the same number of transmitting BS.
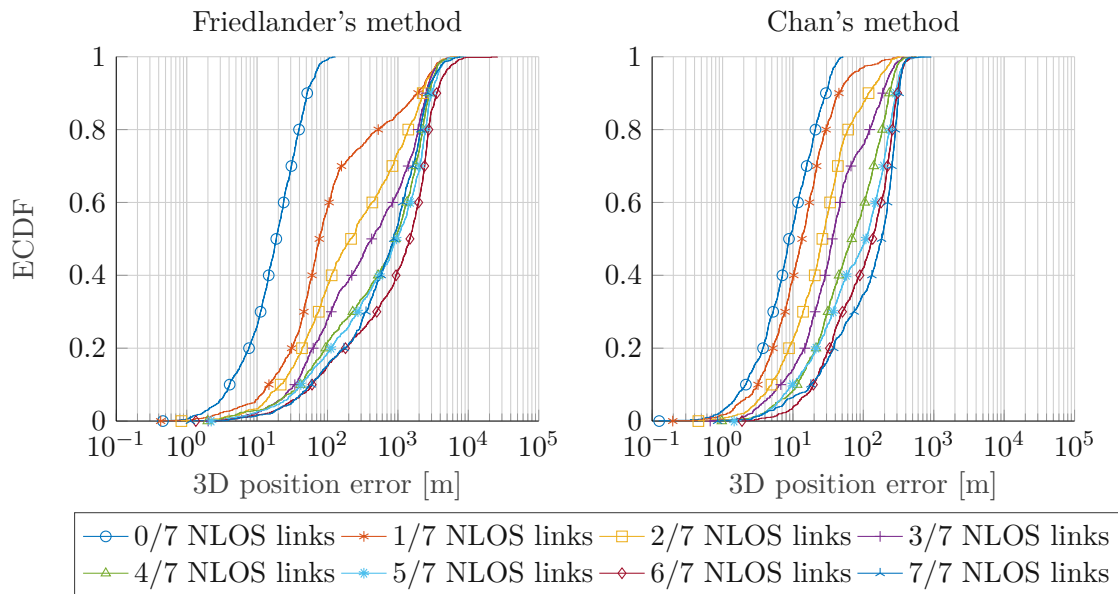
Figure 4.9: UMi scenario, $dim = 3$
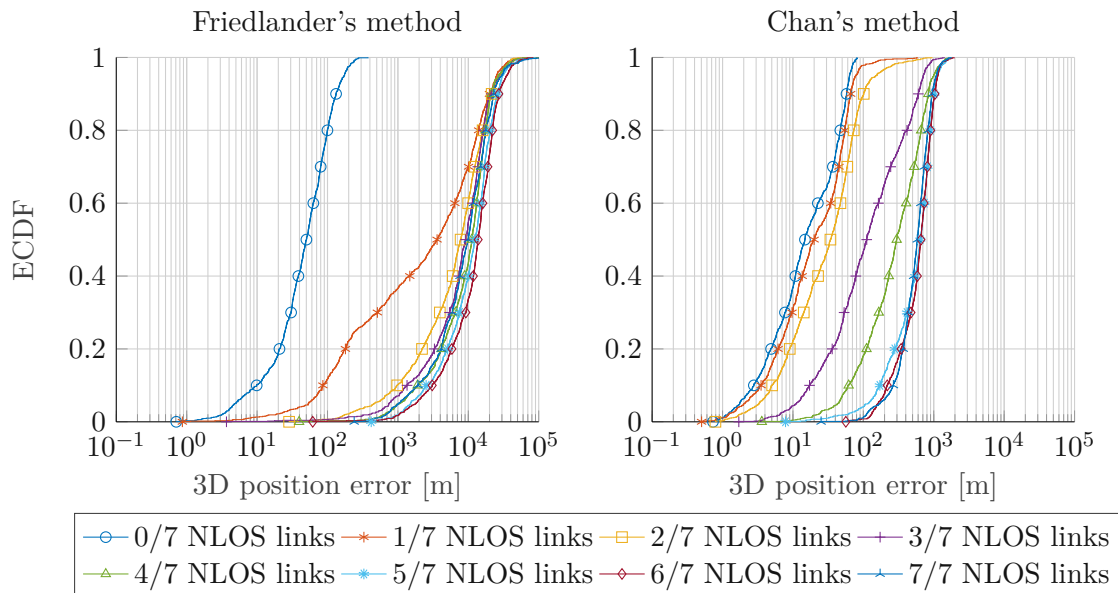
Figure 4.10: UMa scenario, $dim = 3$

CHAPTER 5

Vehicular positioning in an urban scenario

Chapter 3 introduced methods for time delay estimation in NLOS multipath environments and chapter 4 showed how the positioning problem can be solved in cellular networks, especially with unreliable TDOA measurements in mind. The goal of this chapter is to make use of the methods presented in the previous chapters and to apply them to vehicular positioning in a scenario based on the geometry of a real-world location.

This chapter is structured as follows: Section 5.1 introduces the vehicular positioning scenario and section 5.2 summarizes the simulation result and presents an in-depth interpretation of the results.
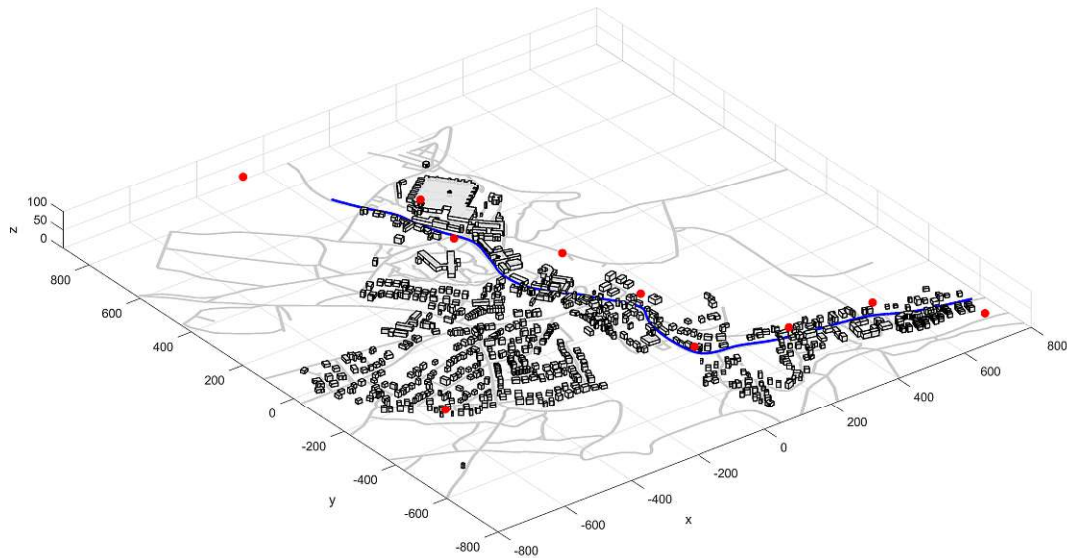
Figure 5.1: Mauerbach scenario layout, red dots signify the 10 BS positions, blue signifies the vehicle's trajectory

5.1   Scenario

For the simulations in this chapter, we select an Austrian town named Mauerbach [MAU] as a basis for the scenario. It is located in the federal state of Lower Austria on the border to Vienna and features a suburban-type settlement placed along a curvy main road. This location was chosen because it features frequent switches between LOS and NLOS for the radio links, which leads to the cellular positioning challenges addressed in the previous chapters. The curvy trajectory leads to further NLOS links and makes it an interesting scenario for sensor fusion, e.g. with radar [AEBM20]. We incorporate some functionalities from the Vienna 5G System Level Simulator [MAD$^+$18] in our simulation framework, which allow us to fetch and use open source street and building geometry data from OpenStreetMap [OSM]. The data obtained by this method is visualized in figure 5.1. Furthermore, the Vienna 5G System Level Simulator provides the ability to compute for any given radio link from any given position if it is LOS or NLOS, hence blocked by a building. This is done by making use of the actual geometry data downloaded from OpenStreetMap. In this scenario, we assume that the cellular receiver is attached to a vehicle in a height of $z_{UE} = 1.5$ m, which is moving at a constant speed of $v = 50$ km/h along the town's main road. The reference positions of the vehicle are obtained by sampling this trajectory at a rate of 10 Hz, as visualized in figure 5.1. Note that the start of the trajectory is close to the right corner of figure 5.1. In the basic simulation scenario we place a total of 10 BSs in the region of interest, with the biggest share being placed along the main road with an inter-station distance of at least 200 m. Variations of

Name	Value
Channel realizations per position	$N_{mc} = 100$
Pathloss model	3GPP UMi
Delay spread	$DS = 129$ ns
Number of BSs	$N_{BS} \in \{6, 10, 30\}$
Transmit power	$P_{tx} = 24$ dBm
BS height	$z_{BS} \in [30, 100]$ m
UE height	$z_{UE} = 1.5$ m
Vehicle speed	$v = 50$ km/h
Positioning rate	10 Hz

Table 5.1: Mauerbach scenario parameters

this scenario decrease the amount of BS to a total of $N_{BS} = 6$ or increase the BS density to $N_{BS} = 30$.

5.2 Simulations

5.2.1 Setup

The simulation framework used in this chapter is similar to the setup introduced in the previous chapter, with some minor tweaks. The common simulation parameters are the same as in table 4.3, while the scenario-specific parameters are listed in table 5.1. Note that the increased BS heights are a result of the location's terrain, as it is located in a valley. For the same reasons as stated in the previous chapter, we employ the time domain correlation method for estimating the propagation delay. In terms of delay peak detection methods, we employ the adaptive threshold detector since we expect many NLOS links. Additionally, we compare it with the maximum peak detector to evaluate what can be gained in this scenario by employing a more advanced method. Furthermore, we introduce a combined detection method, which assumes that perfect knowledge of the LOS condition of all links at the receiver is supplied by an oracle. Hence we refer to this method as *oracle detector*. Since we know from the results in section 3.5 that the maximum peak detector performs best for LOS links and the adaptive threshold detector performs best for NLOS links, we switch the delay peak detection method based on the given LOS condition. In order to estimate the UE position we employ Chan's method, as the simulation results from section 4.3 showed the method's superior performance in NLOS-heavy environments. We also present a performance comparison with Friedlander's method. Note that as in the previous chapter, inter-cell interference free transmission is assumed.
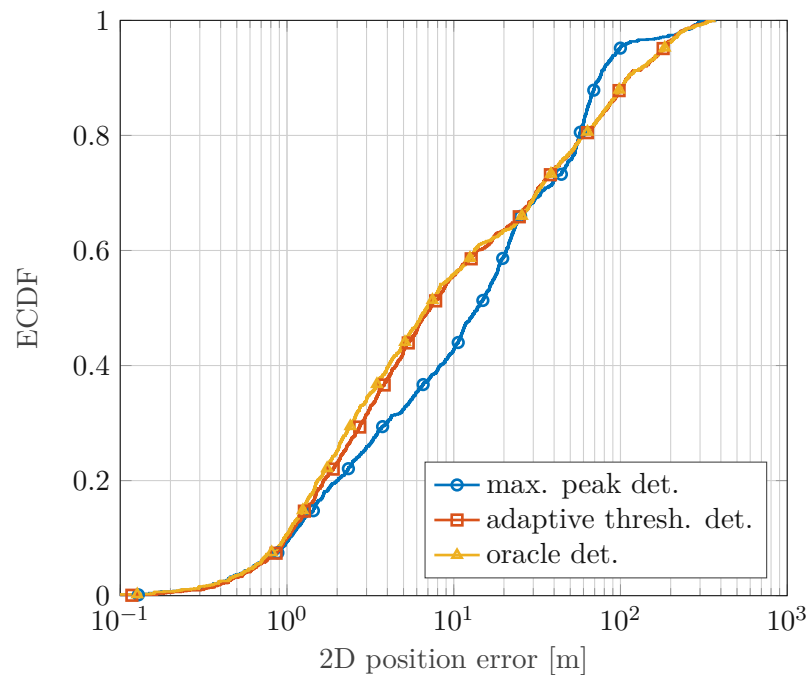
Figure 5.2: Mauerbach scenario, delay peak detection method comparison

5.2.2 Results

The simulation results from this chapter present how the positioning framework introduced by the former chapters performs in a NLOS-heavy scenario based on a real-world location. In figure 5.2, the 2D position error distributions are visualized for different delay peak detection methods. The simulation results depicted in this figure confirm that employing the adaptive threshold detection method in an environment with many NLOS links can improve the positioning accuracy - the error is reduced by almost 50% for 50% of the trajectory (c.f. table 5.2) - as compared to a setup using the naive maximum peak detector. Combining the advantages of both detection methods in the oracle detector yields only little improvement. Interestingly, the distributions overlap for very small positioning errors, which is where the measurements stem from road sections with the highest number of LOS links. Furthermore, we observe that the maximum peak detector is more accurate in the high-error regime. We explain this behavior with situations where the direct path is strongly attenuated and thus the adaptive threshold detector wrongly picks up a noise peak, yielding higher errors than picking the maximum peak. Selected values from the empirical cumulative distribution function (ECDF) curves in figure 5.2 are presented in table 5.2. Variations in the results such as the slighty decreased accuracy of the oracle detector as compared to the adaptive threshold detector for 80% of the values are assumed to be a result of non-perfect measurement confidence weighting in Chan's positioning method and varying channel realizations.

Method	50% ≤	80% ≤	90% ≤
Max. peak det.	13.83 m	56.95 m	74.99 m
Adaptive thresh. det.	7.23 m	59.40 m	110.69 m
Oracle det.	6.87 m	59.73 m	110.25 m

Table 5.2: Selected 2D position error values from the distributions in figure 5.2
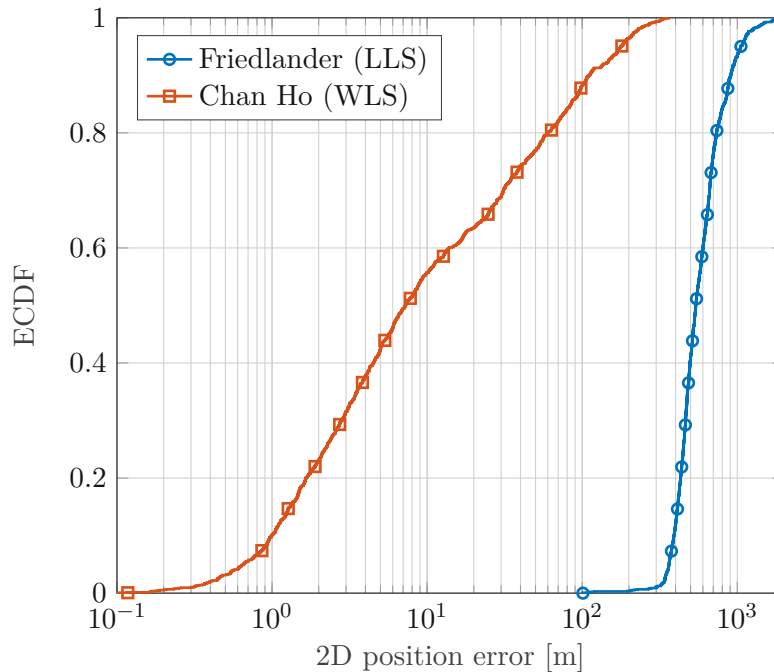
Figure 5.3: Mauerbach scenario, hyperbolic positioning method comparison

Method	50% ≤	80% ≤	90% ≤
Friedlander (linear LS)	540.12 m	736.52 m	907.05 m
Chan Ho (weighted LS)	7.23 m	59.40 m	110.69 m

Table 5.3: Selected 2D position error values from the distributions in figure 5.3

In figure 5.3, the simulation results confirm again that Chan's weighted LS approach is far superior to Friedlander's linear LS method when performing hyperbolic positioning in NLOS-heavy environments with unreliable TDOA measurements. Selected values from the ECDF curves in figure 5.3 are presented in table 5.3.

The simulation results pictured in figure 5.4 clearly show the effect of varying the BS density in the scenario. Selected accuracy values are listed in table 5.4. Significantly increasing the number of BSs from 10 to 30 yields a distribution with significantly lower variance in the 2D positioning error. This is because an increased number of BSs
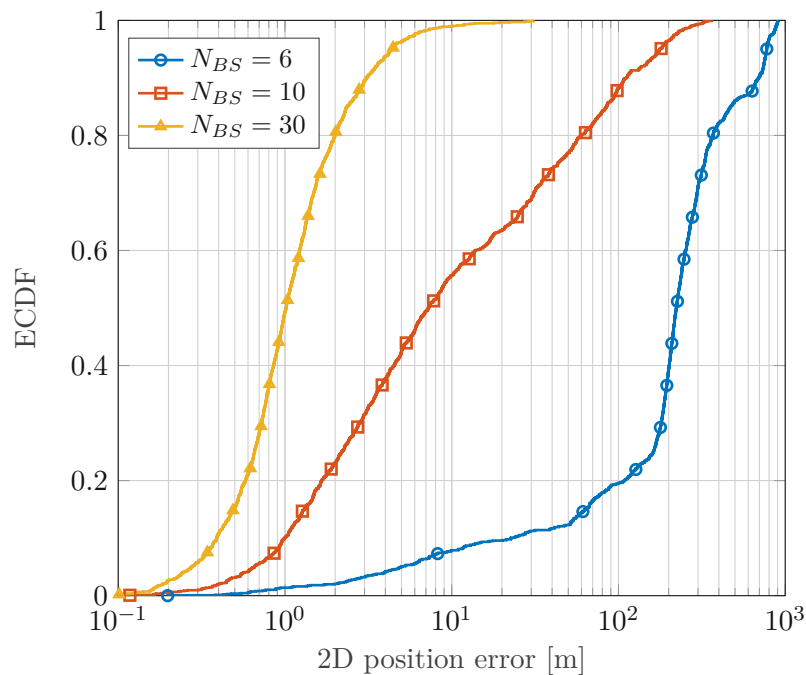
Figure 5.4: Mauerbach scenario, varying N_{BS}

N_{BS}	50% $\leq$	80% $\leq$	90% $\leq$
6	222.27 m	368.52 m	692.69 m
10	7.23 m	59.40 m	110.69 m
30	1.02 m	1.99 m	3.08 m

Table 5.4: Selected 2D position error values from the distributions in figure 5.4

simultaneously increases the propability for high confidence TDOA measurements, both due to more LOS links and more powerful NLOS links. The opposite is observed if the BS density is reduced from 10 to 6 - the number of LOS links available at a specific road section decreases as well as the number of powerful NLOS links, hence leading to a distribution with a large amount of low accuracy values.

Figure 5.5 visualizes the simulated 2D positioning error for every position on the vehicle trajectory. Furthermore, for each position the number of available LOS links is shown, implying that the remaining links are in NLOS for that specific position. Observing both graphs in conjunction reveals a correlation pattern with the following behavior: The positioning accuracy tends to increase with an increasing number of LOS links and decreases with an increasing number of NLOS links. The strongest position error jumps tend to occur in situations where the number of available LOS links switches between 2 and 3. This leads to the observation that our framework requires at least 2-3 LOS links in this scenario to deliver reasonable performance - depending on the BS-UE distances at
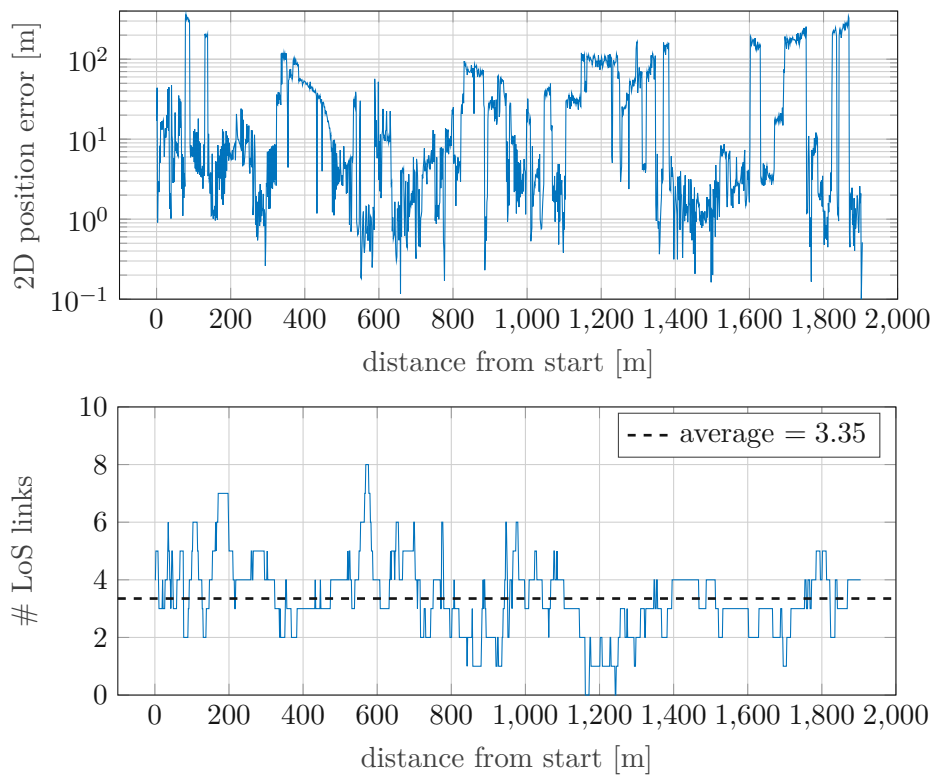
Figure 5.6: Mauerbach scenario, $N_{BS} = 10$, adaptive threshold detector. Note that not all BS positions are shown in this figure.

CHAPTER 6

Conclusion

In this thesis, we argued that multipath propagation and attenuated direct signal paths due to reflections and blockages are prevalent in cellular network transmissions for (sub-) urban vehicular scenarios. Based on that, we identified the need for methods able to accurately measure propagation time delay in NLOS channels for a cellular network vehicular positioning system. Therefore, we investigated different methods suitable for estimating multipath delay profiles with 5G-NR standard-compliant reference signals. Furthermore, we presented methods for estimating the propagation time delay due to the direct path in NLOS channels by detecting the first peak in a delay profile. A MATLAB simulation framework implementing the 5G-NR OFDM transmission system model was developed in order to compare the ranging accuracy of the various methods by employing 3GPP standard-compliant stochastic channel models. The simulation results showed that for LOS channels, the combination of the time domain cross-correlation delay profile and the maximum peak detector methods yields the best ranging performance. For NLOS channels, the simulations revealed that the MUSIC delay profile in combination with the adaptive threshold detector yields the best ranging performance, however with varying results due to difficult threshold tuning in the detection method.

In order to estimate the position of a vehicle, we presented the hyperbolic positioning problem arising from TDOA measurements in cellular networks. We showed two methods for solving the hyperbolic positioning problem, one relying on a simple linear least squares approach without a-priori information and another, employing the weighted least squares method with TDOA value weighting due to measurement confidence. Our MATLAB simulation framework was extended to allow for the modelling of cellular network geometry with multiple transmitting BSs and with standard-compliant path loss models and simulation scenarios. The simulations revealed the clearly superior positioning accuracy of the weighted least squares approach in situations where at least one link is subject to NLOS propagation.

Finally, we modelled a simulation scenario based on the real world geometry of an urban area. For this purpose, we extracted blockage data from OpenStreetMap and used it to compute the LOS/NLOS condition for all radio links on any given point along a predefined vehicular trajectory with our MATLAB framework. This information was used to simulate the vehicular positioning accuracy along the trajectory. The results showed that a 2D position error well below 10 m is feasible with our positioning framework in situations where at least 2-3 LOS links are available, depending on the particular transmission distance. Furthermore, the simulation results revealed that in our scenario periods with a high positioning error are limited to comparably short road sections.

6.1   Future work

The work in this thesis could be extended by investigating various optimizations of the methods outlined in this thesis. Specific hints for possible improvements are given in the respective chapters. A future work could be to take the positioning data along the vehicular trajectory generated by the simulations of an urban scenario and pass it to a filtering method in order to mitigate the sections with low positioning accuracy. Another major extension would be to take the step from performing simulations further to performing real world measurement campaigns. For this it would be crucial to communicate with network providers on how they implement the reference signals required for the methods in this thesis. Furthermore, a challenging task would be to establish a suitable ground truth in order to be able to asses the positioning accuracy of the proposed framework. Finally, such a measurement campaign could also be used to collect positioning data from other methods such as for example GNSS or RADAR. This data would be interesting on the one hand to provide a basis for comparing the performance of the methods and on the other hand to perform sensor fusion.

List of Figures

List of Tables

Acronyms

3GPP 3rd generation partnership project. 3, 6, 12, 15, 30, 31, 39, 47, 48, 63, 65

5G-NR 5th generation cellular network - new radio. 2, 3, 5, 8–12, 15, 21, 25, 39, 63

ADAS advanced driver assistance systems. 1

AOA angle of arrival. 9

AOD angle of departure. 8–10

AWGN additive white gaussian noise. 20, 22, 23, 27, 30, 33, 35, 47, 65

BS base station. 2, 5–11, 23, 39–41, 43–49, 52, 56, 57, 60–63, 66

CFR channel frequency response. 14, 19, 24, 30

CIR channel impulse response. 14, 16–18

D2D device-to-device. 2

DAC digital-to-analog converter. 15

DFT discrete fourier transform. 14, 18

DFT^{-1} inverse discrete fourier transform. 13, 14

ECDF empirical cumulative distribution function. 58

FFT fast fourier transform. 14, 21, 32, 49

FFT^{-1} inverse fast fourier transform. 14

FIR finite impulse response. 17, 18

GNSS global navigation satellite system. 1, 3, 10, 22, 64

TDL tapped delay line. 30, 32, 48

TDOA time difference of arrival. 3, 7–10, 32, 39–42, 44, 46, 50, 52, 55, 58, 60, 63

TOA time of arrival. 7–9, 39, 41

UE user equipment. 5, 6, 8, 9, 11, 13, 39, 40, 42, 44–50, 57, 61

UMa Urban Macrocell. 47–50, 52, 53, 66, 67

UMi Urban Microcell. 32, 47–51, 53, 66, 67

V2I vehicle-to-infrastructure. 2, 3

V2V vehicle-to-vehicle. 2

Bibliography

[AEBM20]   Mehdi Ashury, Christian Eliasch, Thomas Blazek, and Christoph F Mecklenbräuker. Accuracy requirements for cooperative radar with sensor fusion. In *2020 14th European Conference on Antennas and Propagation (EuCAP)*, pages 1–5. IEEE, 2020.

[AST]   Automatische strassenverkehrszählung, bmk/asfinag. `https://www.bmk.gv.at/themen/verkehr/strasse/statistik/automatische-zaehlung.html`. Accessed: 05.10.2022.

[BHL+14]   Federico Boccardi, Robert W Heath, Angel Lozano, Thomas L Marzetta, and Petar Popovski. Five disruptive technology directions for 5g. *IEEE communications magazine*, 52(2):74–80, 2014.

[CH94a]   Yiu Tong Chan and KC Ho. An efficient closed-form localization solution from time difference of arrival measurements. In *Proceedings of ICASSP'94. IEEE International Conference on Acoustics, Speech and Signal Processing*, volume 2, pages II–393. IEEE, 1994.

[CH94b]   Yiu Tong Chan and KC Ho. A simple and efficient estimator for hyperbolic location. *IEEE Transactions on signal processing*, 42(8):1905–1915, 1994.

[dPRLSSG+12] José A del Peral-Rosado, José A López-Salcedo, Gonzalo Seco-Granados, Francesca Zanier, and Massimo Crisci. Achievable localization accuracy of the positioning reference signal of 3gpp lte. In *2012 International Conference on Localization and GNSS*, pages 1–6. IEEE, 2012.

[DSM+21]   Satyam Dwivedi, Ritesh Shreevastav, Florent Munier, Johannes Nygren, Iana Siomina, Yazid Lyazidi, Deep Shrestha, Gustav Lindmark, Per Ernström, Erik Stare, et al. Positioning in 5g networks. *IEEE Communications Magazine*, 59(11):38–44, 2021.

[DZW+20]   Zhongliang Deng, Xinyu Zheng, Hanhua Wang, Xiao Fu, Lu Yin, and Wen Liu. A novel time delay estimation algorithm for 5g vehicle positioning in urban canyon environments. *Sensors*, 20(18):5190, 2020.

[FE08]   Fernando Pærez Fontæn and Perfecto Mariæo Espiæeira. *Modelling the wireless propagation channel: a simulation approach with Matlab*. John Wiley & Sons, 2008.

[Fri87]   Benjamin Friedlander. A passive localization algorithm and its accuracy analysis. *IEEE Journal of Oceanic engineering*, 12(1):234–245, 1987.

[GSPL04]   Feng-Xiang Ge, Dongxu Shen, Yingning Peng, and Victor OK Li. Super-resolution time delay estimation in multipath environments. In *2004 IEEE Wireless Communications and Networking Conference (IEEE Cat. No. 04TH8733)*, volume 2, pages 1121–1126. IEEE, 2004.

[GWK+20]   Yu Ge, Fuxi Wen, Hyowon Kim, Meifang Zhu, Fan Jiang, Sunwoo Kim, Lennart Svensson, and Henk Wymeersch. 5g slam using the clustering and assignment approach with diffuse multipath. *Sensors*, 20(16):4656, 2020.

[IM08]   Cyril-Daniel Iskander and Hi-Tek Multisystems. A matlab-based object-oriented approach to multipath fading channel simulation. *Hi-Tek Multisystems*, 21:1–15, 2008.

[KC76]   Charles Knapp and Glifford Carter. The generalized correlation method for estimation of time delay. *IEEE transactions on acoustics, speech, and signal processing*, 24(4):320–327, 1976.

[KFK+18]   Sampo Kuutti, Saber Fallah, Konstantinos Katsaros, Mehrdad Dianati, Francis Mccullough, and Alexandros Mouzakitis. A survey of the state-of-the-art localization techniques and their potentials for autonomous vehicle applications. *IEEE Internet of Things Journal*, 5(2):829–846, 2018.

[KGG+20]   Hyowon Kim, Karl Granström, Lin Gao, Giorgio Battistelli, Sunwoo Kim, and Henk Wymeersch. 5g mmwave cooperative positioning and mapping using multi-model phd filter and map fusion. *IEEE Transactions on Wireless Communications*, 19(6):3782–3795, 2020.

[KKSM17]   Zaher Zak M Kassas, Joe Khalife, Kimia Shamaei, and Joshua Morales. I hear, therefore i know where i am: Compensating for gnss limitations with cellular signals. *IEEE Signal Processing Magazine*, 34(5):111–124, 2017.

[KSHK19]   Ryan Keating, Mikko Säily, Jari Hulkkonen, and Juha Karjalainen. Overview of positioning in 5g new radio. In *2019 16th International Symposium on Wireless Communication Systems (ISWCS)*, pages 320–324. IEEE, 2019.

76

[KWG+18]   Hyowon Kim, Henk Wymeersch, Nil Garcia, Gonzalo Seco-Granados, and Sunwoo Kim. 5g mmwave vehicular tracking. In *2018 52nd Asilomar Conference on Signals, Systems, and Computers*, pages 541–547. IEEE, 2018.

[LP04]   Xinrong Li and Kaveh Pahlavan. Super-resolution toa estimation with diversity for indoor geolocation. *IEEE transactions on wireless communications*, 3(1):224–234, 2004.

[MAD+18]   Martin Klaus Müller, Fjolla Ademaj, Thomas Dittrich, Agnes Fastenbauer, Blanca Ramos Elbal, Armand Nabavi, Lukas Nagel, Stefan Schwarz, and Markus Rupp. Flexible multi-node simulation of cellular mobile communications: the Vienna 5G System Level Simulator. *EURASIP Journal on Wireless Communications and Networking*, 2018(1):17, September 2018.

[MATa]   Matlab 5g toolbox. `https://de.mathworks.com/help/5g/index.html`. Accessed: 24.08.2022.

[MATb]   Matlab include path loss in nr link-level simulations. `https://de.mathworks.com/help/5g/ug/include-path-loss-in-nr-link-level-simulations.html`. Accessed: 31.08.2022.

[MATc]   Matlab nr positioning reference signal. `https://de.mathworks.com/help/5g/ug/5g-new-radio-prs.html`. Accessed: 01.08.2022.

[MAU]   Mauerbach, openstreetmap. `https://www.openstreetmap.org/#map=16/48.2465/16.1684`. Accessed: 14.09.2022.

[Men13]   Christian Mensing. *Location determination in OFDM based mobile radio systems.* PhD thesis, Technische Universität München, 2013.

[MGA+20]   FJ Mata, F Grec, M Azaola, F Blázquez, A Fernández, E Dominguez, G Cueto-Felgueroso, G Seco-Granados, JA del Peral-Rosado, Emanuel Staudinger, et al. Preliminary field trials and simulations results on performance of hybrid positioning based on gnss and 5g signals. In *Proceedings of the 33rd International Technical Meeting of the Satellite Division of The Institute of Navigation (ION GNSS+ 2020)*, pages 387–401, 2020.

[Mit12]   Harvey B Mitchell. *Data fusion: concepts and ideas.* Springer Science & Business Media, 2012.

77

[MKE+21]   Ivo Müürsepp, Marika Kulmar, Osama Elghary, Muhammad Mahtab Alam, Tao Chen, Seppo Horsmanheimo, and Johan Scholliers. Performance evaluation of 5g-nr positioning accuracy using time difference of arrival method. In *2021 IEEE International Mediterranean Conference on Communications and Networking (MeditCom)*, pages 494–499. IEEE, 2021.

[Mol12]   Andreas F. Molisch. *Wireless communications*. John Wiley & Sons, 2012.

[MSD10]   Christian Mensing, Stephan Sand, and Armin Dammann. Hybrid data fusion and tracking for positioning with gnss and 3gpp-lte. *International Journal of Navigation & Observation*, 2010.

[OSM]   Openstreetmap. https://www.openstreetmap.org. Accessed: 14.09.2022.

[PAK+05]   Neal Patwari, Joshua N Ash, Spyros Kyperountas, Alfred O Hero, Randolph L Moses, and Neiyer S Correal. Locating the nodes: cooperative localization in wireless sensor networks. *IEEE Signal processing magazine*, 22(4):54–69, 2005.

[PP00]   John David Parsons and Prof J David Parsons. *The mobile radio propagation channel*, volume 2. wiley New York, 2000.

[rGPPG18]   3rd Generation Partnership Project (3GPP). Technical Report; Study on channel model for frequencies from 0.5 to 100GHz. TR 38.901 version 14.3.0 Release 14, 3rd Generation Partnership Project (3GPP), January 2018.

[rGPPG20a] 3rd Generation Partnership Project (3GPP). Technical Specification; NG-RAN; Architecture description. TS 38.401 version 16.3.0 Release 16, 3rd Generation Partnership Project (3GPP), November 2020.

[rGPPG20b] 3rd Generation Partnership Project (3GPP). Technical Specification; NR; Physical channels and modulation. TS 38.211 version 16.2.0 Release 16, 3rd Generation Partnership Project (3GPP), July 2020.

[rGPPG22]   3rd Generation Partnership Project (3GPP). Technical Report; Release 16 Description. TR 21.916 version 16.1.0 Release 16, 3rd Generation Partnership Project (3GPP), January 2022.

[Sch86]   Ralph Schmidt. Multiple emitter location and signal parameter estimation. *IEEE transactions on antennas and propagation*, 34(3):276–280, 1986.

78

[STV]   Verkehrsstatistik 2021, bmi.   `https://www.bmi.gv.at/202/`
            `Verkehrsangelegenheiten/unfallstatistik_vorjahr.`
            `aspx`. Accessed: 05.10.2022.

[VT04]   Harry L Van Trees. *Optimum array processing: Part IV of detection,
            estimation, and modulation theory.* John Wiley & Sons, 2004.

[WGZ13]   L Wang, PD Groves, and MK Ziebart. Gnss shadow matching: Improving
            urban positioning accuracy using a 3d city model with optimized visibility
            scoring scheme. *Navigation, Journal of the Institute of Navigation*,
            60(3):195–207, 2013.

[WKWW20]   Fuxi Wen, Josef Kulmer, Klaus Witrisal, and Henk Wymeersch. 5g
            positioning and mapping with diffuse multipath. *IEEE Transactions on
            Wireless Communications*, 20(2):1164–1174, 2020.

[WML+16]   Klaus Witrisal, Paul Meissner, Erik Leitinger, Yuan Shen, Carl
            Gustafson, Fredrik Tufvesson, Katsuyuki Haneda, Davide Dardari, An-
            dreas F Molisch, Andrea Conti, et al. High-accuracy localization for
            assisted living: 5g systems will turn multipath channels from foe to
            friend. *IEEE Signal Processing Magazine*, 33(2):59–70, 2016.

[XHZD16]   Wen Xu, Ming Huang, Chen Zhu, and Armin Dammann. Maximum
            likelihood toa and otdoa estimation with first arriving path detection
            for 3gpp lte system. *Transactions on Emerging Telecommunications
            Technologies*, 27(3):339–356, 2016.

[ZB11]   Reza Zekavat and R Michael Buehrer. *Handbook of position location:
            Theory, practice and advances*, volume 27. John Wiley & Sons, 2011.

[ZLWW17]   Ping Zhang, Jian Lu, Yan Wang, and Qiao Wang. Cooperative localiza-
            tion in 5g networks: A survey. *Ict Express*, 3(1):27–32, 2017.

[ZYLS07]   Fang Zhao, Wenbing Yao, Catharina Carlemalm Logothetis, and
            Yonghua Song. Super-resolution toa estimation in ofdm systems for
            indoor environments. In *2007 IEEE International Conference on Net-
            working, Sensing and Control*, pages 723–728. IEEE, 2007.